DOT/FAA/TC-24/31

Federal Aviation Administration
William J. Hughes Technical Center
Aviation Research Division
Atlantic City International Airport
New Jersey 08405

Analysis of Granular Base/Subbase in Airport Pavements Using Embedded Sensors

September 2024

Final Report

U.S. Department of Transportation
Federal Aviation Administration

NOTICE

Technical Report Documentation Page

1. Report No.	2. Government Accession No.	3. Recipient's Catalog No.
DOT/FAA/TC-24/31		

4. Title and Subtitle	5. Report Date
ANALYSIS OF GRANULAR BASE/SUBBASE IN AIRPORT PAVEMENTS USING EMBEDDED SENSORS	September 2024
	6. Performing Organization Code
7. Author(s)	8. Performing Organization Report No.
Erol Tutumluer, Mingu Kang, and Issam I. A. Qamhia	
9. Performing Organization Name and Address Department Civil and Environmental Engineering University of Illinois Urbana-Champaign 205 N. Mathews, Urbana, IL 61801	10. Work Unit No. (TRAIS)
	11. Contract or Grant No. 692M15-19-T-00023
12. Sponsoring Agency Name and Address U.S. Department of Transportation Federal Aviation Administration Airport Engineering Division 800 Independence Ave., SW Washington, DC 20591	13. Type of Report and Period Covered Final Report
	14. Sponsoring Agency Code AAS-110

15. Supplementary Notes
The Federal Aviation Administration Aviation Research Division COR was Dr. Navneet Garg.

16. Abstract

This project investigates the modulus and deformation behavior of granular base/subbase layers in airport pavements using three types of embedded sensors: bender element (BE) field sensors, coil sensors, and pressure cells. These sensors were installed in multiple test items at the Federal Aviation Administration's Construction Cycle 9 (CC9) of the National Airport Pavement Test Facility (NAPTF). This report discusses the sensor instrumentation procedure, data collection during pre-traffic and traffic tests, and the analysis of measured data.

The objective of this research was to monitor and analyze the in situ resilient modulus characteristics of the constructed aggregate base layer using BE field sensors throughout the six test stages, including five pre-traffic test stages and the main traffic test stage, with realistic aircraft loading patterns. Additionally, researchers analyzed the deformation behavior of the granular base by collecting data from arrays of coil sensors installed in the depth profile. The experiment investigated the influence of load wander patterns, the impact of dynamic loading on base moduli, deformation characteristics of the granular base with depth, and the effect of geogrid stabilization on stiffness based on sensor measurements and analyses.

The findings of the NAPTF CC9 experiment were that embedded sensors serve as effective tools for monitoring and evaluating the behavior of granular base/subbase layers in airport pavements under various loading conditions.

17. Key Words	18. Distribution Statement
Granular base/subbase layers, Airport pavements, Resilient modulus, Stiffness, Unbound aggregates, Embedded sensors, Bender element (BE) sensors, Inductive coil sensors, Pressure cells, Vehicle wander, Pavement deformation, Construction Cycle 9 (CC9), National Airport Pavement Test Facility (NAPTF), Sensor instrumentation, Data collection, Deformation behavior, Aircraft loading, Dynamic loading, Geogrid stabilization	This document is available to the U.S. public through the National Technical Information Service (NTIS), Springfield, Virginia 22161. This document is also available from the Federal Aviation Administration William J. Hughes Technical Center at actlibrary.tc.faa.gov.

19. Security Classif. (of this report)	20. Security Classif. (of this page)	21. No. of Pages	22. Price
Unclassified	Unclassified	72	

ACKNOWLEDGEMENTS

This publication presents the results of Grant # DOT FAA 692M15-19-T-00023: *Bender Element and Coil Sensor Data Driven Approach for Analyzing Modulus and Deformation Behavior of Granular Base/Subbase Layers in Airport Pavements: NAPTF CC9 Tests*. The 692M15-19-T-00023 project was a collaborative effort involving the Illinois Center for Transportation and the U.S. Department of Transportation, Federal Aviation Administration.

The support of the following individuals is gratefully acknowledged:

• Dr. Navneet Garg, Federal Aviation Administration
• Wilfredo Villafane, Federal Aviation Administration
• Scott D. Murrell, Applied Research Associates (ARA)
• Dr. Hasan Kazmee, Applied Research Associates (ARA)

TABLE OF CONTENTS

		Page
EXECUTIVE SUMMARY		xi
1.	INTRODUCTION	1
1.1	Background	1
1.2	Research Need and Objective	4
2.	BENDER ELEMENT INSTRUMENTATION AND DATA ANALYSIS FOR THE GEOSYNTHETIC EXPERIMENT	5
2.1	Bender Element Field Sensor Optimization and Instrumentation	5
2.1.1	Initial Design of BE Field Sensor	5
2.1.2	Optimizing Coaxial Cable	7
2.1.3	Improving BE Plate Design	7
2.1.4	Measurement System for BE Field Sensors	8
2.1.5	Bender Element Field Sensor Instrumentation	9
2.2	Shear Wave Velocity Measurements during Pre-Traffic Tests	15
2.2.1	Test Procedure	15
2.2.2	Results and Discussion	18
2.3	Shear Wave Velocity Measurements during Traffic Tests	24
2.3.1	Laboratory Tests to Convert BE Modulus to Resilient Modulus	24
2.3.2	Procedure for NAPTF Traffic Tests	27
2.3.3	Airport Pavement Base Layer Stiffness Characteristics using BE Field Sensor	29
2.4	SUMMARY	32
3.	COIL SENSOR INSTRUMENTATION AND DATA ANALYSES FOR THE P-209MR LAYER	33
3.1	Coil Sensors	33
3.2	Fatigue Model for LFS-1	34
3.2.1	P-209 Layer Deformation at LFS-1S	34
3.2.2	P-209 Layer Deformation at LFS-1N	38
3.3	Vertical Strain Influence Factor Model for P-209 Base Layer	40
3.4	LFC-3S Geosynthetics and LFC-4S Cement-Treated Drainable Base	42

3.5 Summary 45

4. MODULUS QUANTIFIED USING COIL SENSOR AND PRESSURE CELL DATA FOR P-209 BASE AND P-154 SUBBASE LAYERS 45

4.1 Modulus Calculation using Coil Sensor and Pressure Cell 45
4.2 LFC-3 P-209 Base Layer 46
4.3 LFC-3 P-154 Subbase Layer 48
4.4 Summary 52

5. SUMMARY AND CONCLUSIONS 53

6. REFERENCES 54

LIST OF FIGURES

Figure		Page
1	Plan View and Profile Views of the North and South Sections for the NAPTF CC9 Experiments	2
2	Rut Profile Development from an Offset Wheel	3
3	Bender Element Field Sensor: Photo of the BE Field Sensor, BE Protection Casing Module Filled with Coupling Materials, a Plastic Casing with a Rubber Mount and a BE Inside, and a BE Installed in the Casing Module	6
4	Bender Element Plates during Manufacturing with and without Silver Conductive Paint	8
5	The BE Field Sensor Measurement System	9
6	The CC9 LFC-3 Test Sections showing Plan View and Profile Views of the BE Sensors Installed in the North Section and the BE Sensor Installed in the South Section	10
7	Aggregate Material Properties for NAPTF CC9: Grain-Size Distribution Curve and Moisture–Density Curve	10
8	Photographs of BE Field Sensor Installation at NAPTF CC9 showing Marking Sensor Location, Removing Constructed Aggregates, Preparing the Trench for Cables, Placing BE Sensor, Measuring the Placement Depth, and Preliminary Compaction using a Plate	12
9	Shear Wave Signals for Stage I BE 1 and BE 2, and Stage II BE 1, BE 2, and BE 3	13
10	Shear Wave Signals After Construction of HMA for BE 1, BE 2, and BE 3	14
11	Load Module and Vehicle Loading Sequence for the NAPTV showing the NAPTV Load Module, the NAPTV Load Module Configuration, the Slow-Roll Sequence, and the Proof-Roll Sequence	18
12	Typical Shear Wave Signals during Test No. 5 at the North and South Sections	19
13	Shear Wave Velocity during Static Loading showing Position of the Sensor and the Loading Modulus during Test Nos. 2 and 5 and Variations in V_s with Static Wheel Loading	20
14	Shear Wave Signals Collected during Slow-Roll Test from BE 1 and BE 2	21
15	Variations in V_s during Slow-Roll Testing shown with Dynamic Wheel Load Location for BE 1 After Each Wheel Pass and BE 2 After Each Wheel Pass	22

16	The Effect of Consecutive Wheel Passes on an Unbound Aggregate Base Considering Offset Load Wander Applied at the Previous Pass	23
17	Effect of Moving Wheel Load on V_s	23
18	UI-FastCell Test Configuration and Loading Pulses during Repeated-Load Triaxial Tests	25
19	Resilient Modulus for the P-209 Crushed Aggregate Material	26
20	Bender Element Measurements during Repeated Load Triaxial Test: Shear Wave Signals and Shear Wave Velocities Graphed with Bulk Stress	26
21	Correlation Between Resilient Modulus and Small-Strain Elastic Modulus	27
22	Loading Procedure for NAPTV Traffic Testing showing Dual-Tridem Load Module Gear Configuration and Wheel Tracks Arranged in Nine Wander Positions Applied to the South Section	28
23	Shear Wave Signals Collected during the Traffic Test at LFC-3S	29
24	Shear Wave Velocities and Resilient Moduli Obtained from BE Field Sensor during Traffic Test at LFC-3S	30
25	Shear Wave Signals Collected during the Traffic Test at LFC-3N	31
26	Shear Wave Velocities and Resilient Moduli Obtained from BE Field Sensor during Traffic Test at LFC-3N	32
27	Comparison Between Resilient Moduli from LFC-3S and LFC-3N	32
28	Embedded CSs showing the CS Pairs and the Calibration Device	34
29	Cross-Sections of LFS-1N and LFS-1S	35
30	Accumulated Layer Deformation at LFS-1S P-209 Base Layer	36
31	Change in Distance Between Coil Pairs vs Number of Passes at the P-209 Base Layer of LFS-1S	37
32	Accumulation Trends of Permanent Deformation for Each 3-in. Interval at P-209 Base Layer of LFS-1S	37
33	Accumulated Layer Deformation at LFS-1S P-209 Base Layer	38
34	Change in Distance Between Coil Pairs vs Number of Passes at the P-209 Base Layer of LFS-1N	39

35	Accumulation Trends of Permanent Deformation for Each 3-in. Interval at the P-209 Base Layer of LFS-1N	39
36	P-209 Base Layer Deformations with a 3-in. Interval for LFS-1N and LFS-1S after 26,400 Passes	41
37	Base-Layer Deflection for LFS-1N with Strain Influence Factor Diagram	42
38	Cross-Section View of LFC-3S and LFC-4S	43
39	Distance Between Each Coil Pair at the LFC-3S Section	44
40	Distance Between Each Coil Pair at LFC-4S Section	44
41	Embedded Sensors at NAPTF CC9: Inductive CS Pairs and PC	46
42	Typical Dynamic Responses from Embedded Sensors showing the CS and PC Measurements during Pass 11	47
43	Resilient Moduli Estimated from Embedded Field Sensors during the CC9 Traffic Test for LFC-3 P-209 Base Layer	48
44	Cross-Sections of LFC-3 Showing Embedded Sensors in Subbase Layer for the LFC-3N Geogrid Stabilized and the LFC-3S Unstabilized Control Sections	49
45	Properties for the P-154 Subbase Coarse Aggregate: Grain-Size Distribution and Moisture-Density Relationship	49
46	Traffic Loading Procedure with Wander Patterns for LFC-3N and LFC-3S Test Sections	50
47	Resilient Moduli Estimated using CS-PC Method: Moduli from Track 2 of LFC-3N and Track -2 of LFC-3S	51
48	Resilient Moduli Estimated using CS-PC Method: Moduli from Track 3 of LFC-3N and Track -3 of LFC-3S	52

LIST OF TABLES

Table		Page
1	Comparison of Properties of Coaxial Cables	7
2	Shear Wave Velocity, Small-Strain Elastic Modulus, and Resilient Modulus during and after the Construction	15
3	Loading Test Conditions	16
4	Model Parameters for Determining V_s from Static Wheel Load	20
5	Effect of Geogrid Stabilization Throughout the NAPTF Pre-Trafficking Tests	24
6	Details of the Wander Pattern Applied with the NAPTV during Traffic Testing	28

LIST OF ACRONYMS

3D	Dual-wheel tridem-axle gear configuration
AASHTO	American Association of State Highway and Transportation Officials
AC	Advisory Circular
APT	Accelerated pavement testing
ASTM	American Society for Testing and Materials
BE	Bender element
CAPTIF	Canterbury Accelerated Pavement Testing Indoor Facility
CC	Construction cycle
CS	Coil sensor
CS-PC	Coil sensor and pressure cell
D	Dual-wheel single-axle gear configuration
FAA	Federal Aviation Administration
HMA	Hot mix asphalt
LFC	Low-Strength Subgrade / Flexible Pavement / Conventional Base
LFS	Low-Strength Subgrade / Flexible Pavement / Stabilized Base
MDD	Multi-depth deflectometer
M_R	Resilient modulus
NAPTF	National Airport Pavement Test Facility
NAPTV	National Airport Pavement Test Vehicle
OMC	Optimum moisture content
PC	Pressure cell
PE	Polyethylene
PVC	Polyvinyl chloride
UIUC	University of Illinois Urbana-Champaign
USCS	Unified Soil Classification System
V_S	Shear wave velocity

EXECUTIVE SUMMARY

In the National Airport Pavement Test Facility (NAPTF) Construction Cycle 9 (CC9) experiments, researchers constructed 10 flexible pavement test items in December 2019. These included the fatigue model test (Low-strength subgrade/flexible pavement/stabilized base [LFS]-1), base thickness test (LFS-2), geosynthetics test (Low-strength subgrade/flexible pavement/conventional base [LFC]-3), cement-treated drainable base test (LFC-4), and overload test (LFC-5). These test items were further divided into north and south sections, each with unique cross-sections.

The research team embedded multiple types of sensors within these test sections to measure how the pavement responds to aircraft loading during various loading stages. This report specifically focuses on the data obtained from bender element (BE) field sensors, coil sensors (CSs), and pressure cells (PCs) installed in the base and subbase layers of the three test sections: LFS-1, LFC-3, and LFC-4.

Within LFC-3, three BE field sensors were installed in the base layer. In the LFS-1 north and south sections, the LFC-3 south section, and the LFC-4 south section, arrays of coil sensors were placed in the base layer. Additionally, PCs and a pair of CSs were installed at the top of the base and subbase layers in these three test sections.

This report presents the findings obtained from an investigation into the modulus and deformation behavior of granular base/subbase layers in airport pavements, using data collected from these three types of embedded sensors.

The in situ resilient modulus of the aggregate base layer was evaluated during sensor installation, and during pre-traffic and traffic tests, and compared using two analysis methods: (1) backcalculation using shear wave velocities measured from the BE field sensors and an established correlation linking shear wave velocity and layer density to small strain modulus and then resilient modulus, and (2) direct calculation using the in situ deformations measured using CSs and vertical wheel load stresses measured from PCs. Resilient moduli estimated via shear wave velocities measured with the BE sensors at multiple levels of static loading have shown a stress-hardening behavior of the unbound base layer. From the BE sensor measurements after traffic loading, obtained at various offset distances from the sensor location, a dilative or compressive behavior of the aggregate base layer owing to vehicle wander was demonstrated. The moving wheel dynamic tests with predefined load wander patterns contributed to some stiffness loss of the unbound aggregate layer after the first wander sequence of the traffic test due to particle rearrangement, confirming the “anti-shakedown” effect, which was reported by earlier studies in NAPTF pavement test sections. The base layer modulus from the BE sensor data showed a gradual recovery when the sections were loaded up to 10,000-wheel passes owing to the stabilization and consolidation of the granular material. The moduli estimated during traffic tests from (1) the BE field sensors and (2) the combined data from the CS and PC sensors, were within typical modulus ranges of unbound aggregates used in base layers. The estimated subbase moduli from the geogrid-stabilized section were approximately 70%–150% higher than those from the unstabilized section (estimated using the CS-PC method), suggesting the presence of a stiffened zone in the vicinity of geogrid.

Vertical CS arrays provided data on deformation behavior of thick granular layers. The CS data indicated an initial constant increase of base layer deformation, followed by a steady-state zone as the pavement base layer stabilized and consolidated with traffic loading. The CC9 results confirm previous NAPTF findings indicating that most of the permanent deformation observed at the surface was generated in the thick unbound aggregate base course layers as opposed to the surface or subgrade layers. The maximum permanent deformation occurred near the bottom of the base layer in both LFS-1 test items. Permanent deformation data measured at 3-in. increments via CS arrays revealed that the vertical strain influence factor concept applies to unbound aggregate layers subjected to heavy dynamic aircraft gear loadings.

Based on the NAPTF CC9 data, the BE system was effective for investigating modulus and deformation behavior of granular base/subbase layers in airport pavements under various loading conditions.

1. INTRODUCTION

1.1 BACKGROUND

The Federal Aviation Administration (FAA) built the National Airport Pavement Test Facility (NAPTF) to generate full-scale testing data to investigate the performance of airport pavements subjected to complex gear loading configurations of new generation aircraft. The NAPTF consists of a 900-ft-long and 60-ft-wide test track along with a rail-based test vehicle (National Airport Pavement Test Vehicle, NAPTV) consisting of two carriages. Each carriage is equipped with five independent load modules, and each load module can develop up to 150,000 pounds force on either dual (D) or single (S) wheels, up to a total load capacity of 1.3 million pounds. The NAPTF can simulate various combinations of landing gear and wander sequences at full scale. Test sections are trafficked at a travel speed between 3–5 mph, which represents aircraft taxiing from the gate to the takeoff position. Full-scale tests at the NAPTF are organized by Construction Cycles (CCs). Data on CC1–CC9 are available at the NAPTF web page: https://www.airporttech.tc.faa.gov/NAPTF.

NAPTF Construction Cycle 9 (CC9) consists of 10 flexible pavement test items (Figure 1):

- Fatigue model and base thickness test (LFS-1 and LFS-2, north and south)
- Geosynthetics test (LFC-3 north and south, and LFC-4 south)
- Cement-treated drainable base test (LFC-4 north and south)
- Overload test (LFC-5 north and south)

All test areas are divided into north and south sections having unique cross-sections. The sections are installed over a subgrade with a California Bearing Ratio (CBR) of 5%. LFS refers to Low-strength subgrade Flexible pavement with Stabilized base, and LFC is the Low-strength subgrade Flexible pavement with Conventional base. CC9 test items were constructed between stations (STA) 0+00 and 3+00 (where stationing originates at the west end of the NAPTF building). Each test item is 33 ft wide and 45 ft long, with 15-ft-long transition areas between test items, as shown in Figure 1.

The failure models currently used in FAA's flexible pavement thickness design procedures consider the maximum vertical strain on top of subgrade (for rutting) and maximum horizontal strain at the bottom of all asphalt layers (for cracking) as the failure criteria as defined in Advisory Circular (AC) 150/5320-6G (FAA, 2021). Though subgrade rutting is taken as the controlling mode of structural shear failure, full-scale test data have shown that most of the pavement surface rut is generated in the unbound granular layers, while the subgrade rutting is minimal (Garg et al., 2012; Garg & Hayhoe, 2008; Sarker et al., 2019; Sarker & Tutumluer, 2018). This behavior of the unbound layers can be attributed to loading effects including load wander. This is in accordance with the NAPTF full-scale test data, which already indicated such detrimental effects of load wander on the rutting performance of unbound granular layers (Hayhoe, 2004; Hayhoe et al., 2012). It was found that some of the residual deformation caused by a single pass was recovered due to subsequent load applications offset by wander during a complete trafficking wander that included a sequential wander pattern covering approximately 82% of all traffic from a standard normal distribution curve of real world taxiway traffic

(Hayhoe, 2004; Hayhoe et al., 2012). Figure 2 provides a simple diagram of the observed behavior and shows how stress applied on a soil element offset from a load can change with a moving wheel.

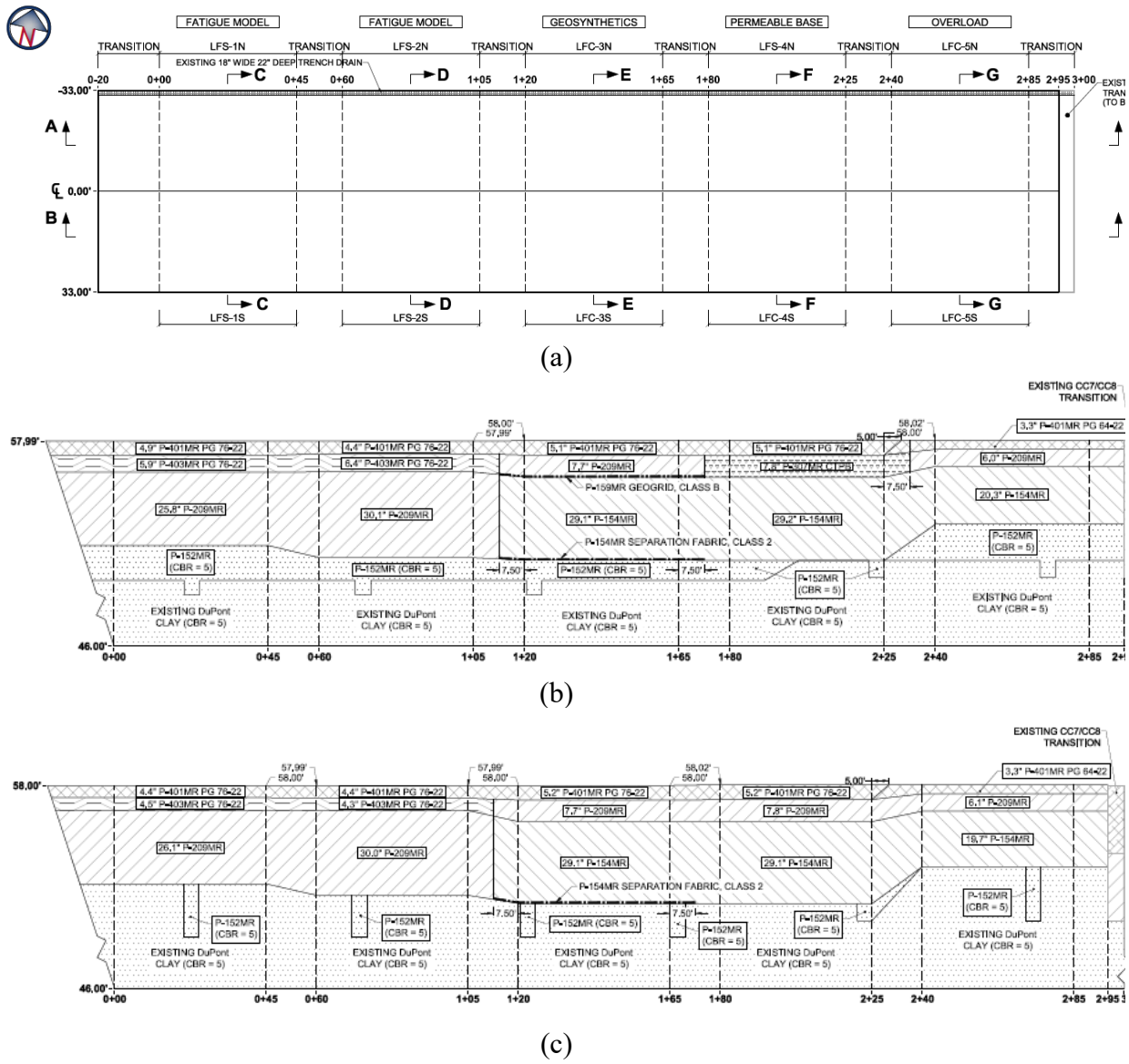

(a)

(b)

(c)

Figure 1. Plan View (a) and Profile Views of the North (b) and South (c) Sections for the NAPTF CC9 Experiments

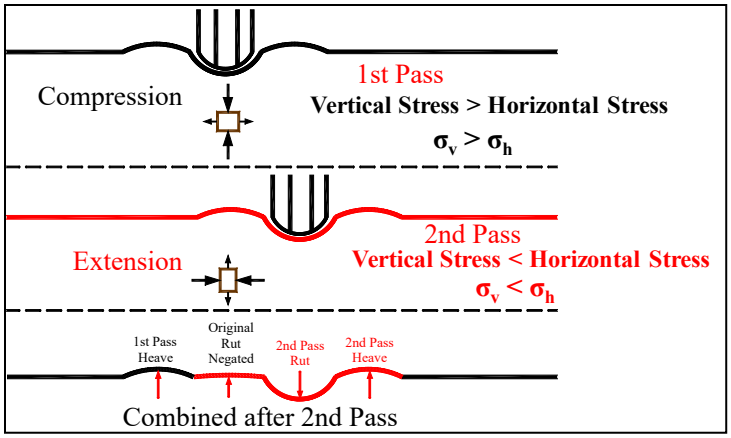

Figure 2. Rut Profile Development from an Offset Wheel

Dynamic pavement response studies conducted at the University of Illinois Urbana-Champaign (UIUC) indicated that unbound aggregate particles moved/rearranged with each gear/wheel pass because of the constantly changing load application lane (Donovan, 2009; Donovan & Tutumluer, 2008; Tutumluer, 2008). This movement negated the consolidation or shakedown expected in unbound aggregate layers under continuous loadings. These findings were further confirmed by the comparison of non-wandered and wandered traffic from the NAPTF CC3 test results, which showed that traffic with wander was more detrimental to the unbound aggregate layers (Donovan, 2009).

Stress history, referring to how any past wheel load applications in the vicinity of the wheel path could influence current conditions, can be an impactful consideration. If a previous pass resulted in the same type of residual deformation as the current one, then the current pass's residual deformation is reduced. This reduction is achieved by multiplying the residual deformation value of the current pass by a constant factor, which is determined based on multipliers for return passes. This attempt at using the influence of the previous pass on the current one, defined as "method of critical points," has been found to be strongly promising (Donovan et al., 2016). The advantage of using the stress history correction procedure is that any combination of wander positions can be simulated to predict the future deformation basin.

However, the application of this method remained very case-specific as the developed model had only limited success in determining the transverse surface rutting profiles of NAPTF Construction Cycle 5 (CC5) (Sarker et al., 2019; Sarker & Tutumluer, 2018). While this approach could predict the deformations in the CC5 test sections at the most trafficked location on the pavement, it could not predict the complete transverse surface profiles of the pavement sections due to the complexities arising from factors such as random loading sequences, complex landing gear configurations, and vehicle wander (Sarker, 2020; Sarker et al., 2019; Sarker & Tutumluer, 2018). Despite showing initial promise, using the "stress history" approach to predict permanent deformation reliably in airport flexible pavements remains a challenge.

A recently completed experiment at the UIUC presented a new surface rut prediction framework for predicting granular-layer permanent-deformation damage accumulation trends in flexible airfield pavements subject to realistic aircraft traffic loading (Sarker & Tutumluer, 2020). This

was achieved by analyzing and modeling the database of the NAPTF CC5 full-scale test sections. Using the CC5 database, the previously developed "stress history effects" method built on CC1 and CC3 was modified. The modified method was used to establish a rut prediction model of CC5 test sections as follows: First, critical wander locations were established and their contributions to transverse rut profiles were studied for multiple passes. Then, by combining measured multi-depth deflectometer (MDD) data, individual pavement layer deformations, and transverse field surface profiles, the researchers developed the rut prediction model for CC5. The developed rut prediction method by Sarker & Tutumluer (2020) is completely data driven and can consider any random path and wander pattern of an airplane traveling on a taxiway/runway to predict the shapes and magnitudes of pavement surface deformation profiles.

In the NAPTF CC9 experiments, FAA shifted from MDDs to inductive coil sensors (CSs) for measuring resilient and permanent deformation in the unbound aggregate base and subbase layers. An inductive coil consists of a circular plastic disk with a groove cut into the perimeter in which a copper wire is wound to form an inductive circuit. Based on 40 years of full-scale pavement instrumentation and testing at the New Zealand's Canterbury Accelerated Pavement Testing Indoor Facility (CAPTIF), the inductive coils used as pairs for pavement instrumentation in vertical and horizontal directions have had success in measuring elastic and plastic strains in unbound aggregate layers (Greenslade et al., 2012). The NAPTF CC9 experiments included inductive CSs manufactured according to the guidelines of the CAPTIF studies, and installed in the vertical direction within (1) 26- to 30-in.-thick P-209MR subbase of the P-209MR layer thickness experiment, (2) 8-in.-thick P-209MR base and 29-in.-thick P-154MR subbase layers of the geosynthetics and cement-treated drainable base experiments, and (3) on top of subgrade in all pavement test sections.

1.2 RESEARCH NEED AND OBJECTIVE

The main objectives of the CC9 experiment were to:

1. Verify/refine/modify the FAA's airfield thickness design program FAARFIELD fatigue model based on the ratio of dissipated energy change,
2. Compare the sensitivity of the FAARFIELD design model to the thickness of subbase material,
3. Investigate the effect of geosynthetics on flexible pavement performance,
4. Evaluate the performance of P-307 cement-treated drainable base course, and
5. Conduct a follow-up to the CC7 test, which identified limiting subgrade vertical strain as a possible design criterion and generated data to support the development of strain criterion for allowable overload in the flexible pavement.

Supporting these objectives, the CC9 experiment specifically investigated the effect of geosynthetic inclusion on unbound aggregate base behavior. In addition, the CC9 experiment also included another test item that focused on the deformation trends of unbound aggregate layers studied through embedded coil sensor data analysis.

The FAA Reauthorization Act of 2018, Section 525 on Geosynthetic Materials, required that the FAA, to the extent practicable, shall encourage the use of durable, resilient, and sustainable materials and methodologies. This includes the use of geosynthetic materials and other

innovative technologies in carrying out FAA activities. As such, both LFC-3N and LFC-3S pavement sections now include an installed geotextile at the subgrade and P-154MR subbase layer interface. Moreover, the LFC-3N test section incorporates an additional biaxial geogrid installed at the P-209MR base and a P-154MR subbase-layer interface to serve the mechanical stabilization function. Mechanical stabilization of unbound aggregate layers involves creating a geogrid-aggregate-stiffened zone with higher confinement. It is essential to be able to measure this stiffened zone associated with the lateral restraint mechanism, and to quantify the benefits of using geogrids, which could include less accumulated permanent deformation and increased pavement service life.

As part of this project, the FAA collected data from BE sensors and inductive coils, which provided the layer modulus and vertical strain data, respectively, during the NAPTF CC9 experiments. This data collection establishes a data-driven approach for the analyses of modulus and deformation behavior of the P-209MR granular base and the P-154MR subbase layers. A full-scale database will be generated, with separate sections dealing with the P-209MR layer thickness experiment, geosynthetics experiment, and the cement-treated drainable base experiment. The research will establish granular base/subbase load distribution mechanisms, and modulus and deformation trends in unstabilized (control) and geogrid-stabilized airport flexible pavement test sections with thick subbase course layers. Identifying the layer modulus characteristics and load-deformation trends in base, subbase, and subgrade due to complex but controlled full-scale gear loads will lead to the development of new and effective airport pavement designs and construction technologies, including geosynthetics and cement-treated drainable aggregate layers.

2. BENDER ELEMENT INSTRUMENTATION AND DATA ANALYSIS FOR THE GEOSYNTHETIC EXPERIMENT

2.1 BENDER ELEMENT FIELD SENSOR OPTIMIZATION AND INSTRUMENTATION

2.1.1 Initial Design of BE Field Sensor

Characterization of soils and aggregates using the propagation of small-strain elastic waves is a small perturbation phenomenon that can assess the state of a particulate medium without altering the structure of the soil or causing permanent effects (Santamarina, 2001). A BE is composed of two layers of piezoceramic plates bonded to a thin metal shim sandwiched in the middle. BE can be used as a shear wave actuator by converting an applied electrical voltage across the BE to a deformation of the BE. Further, the deformation of the BE generates an electric voltage, and thus the BE can also be used as a shear wave sensor. Due to the superiority of coupling between the transducer and soil or aggregates, BEs have been widely used in laboratory applications to instrument soils (Lee & Santamarina, 2005). There are two types of BEs: series and parallel. In the series type, the poling directions of the two piezoelectric layers are opposite to each other; whereas the parallel type has the same poling direction for the two piezoelectric layers. In this experiment, the parallel type was used because it can provide a higher magnitude of shear wave signals. The BEs in this experiment were 1.2 in. long, 1.0 in. wide, and 0.02 in. thick.

Although BEs have an exceptional coupling ability with dense-graded granular materials, these sensors have not been frequently used in the field due to their fragility. To protect a pair of BEs

and their cable connections from potential damage during construction, and to ensure that the BE sensors are directly facing each other during a shear wave signal propagation, a new BE field sensor has been developed at UIUC for transportation geotechnics field applications. Figure 3 shows a single BE, a BE sensor with a BE protection casing module, and the final design of the BE field sensor used in this experiment. To protect the BE sensor, an aluminum mesh cover was used to cover the BE protection module. A stainless-steel frame enables the installation of the BE field sensor in a coarse aggregate base layer-type dense-grade material size and gradation without damaging the sensors and cables. The frame also maintains a fixed distance between the two pairs of BEs. The frame was 4 ft long and 1.5 ft wide. The length was designed to be longer than the width of the gears/tires used to traffic the pavement, and the width was optimized to ensure that a clear shear wave could be generated and detected without any interference from the stainless-steel frame. The BE protection module was first filled with a coupling material engineered to be a uniform coarse sand so that shear waves could be propagated in a continuous medium. The BE protection module was approximately 2.4 in. thick. To minimize the possibility of a direct shear wave propagating through the frame, a rubber mount was attached to the BE protection module. Diagonal support bars were fitted at the four corners of the sensor frame to prevent out-of-plane warping and to ensure both BEs were in the same plane (Kang et al., 2021).

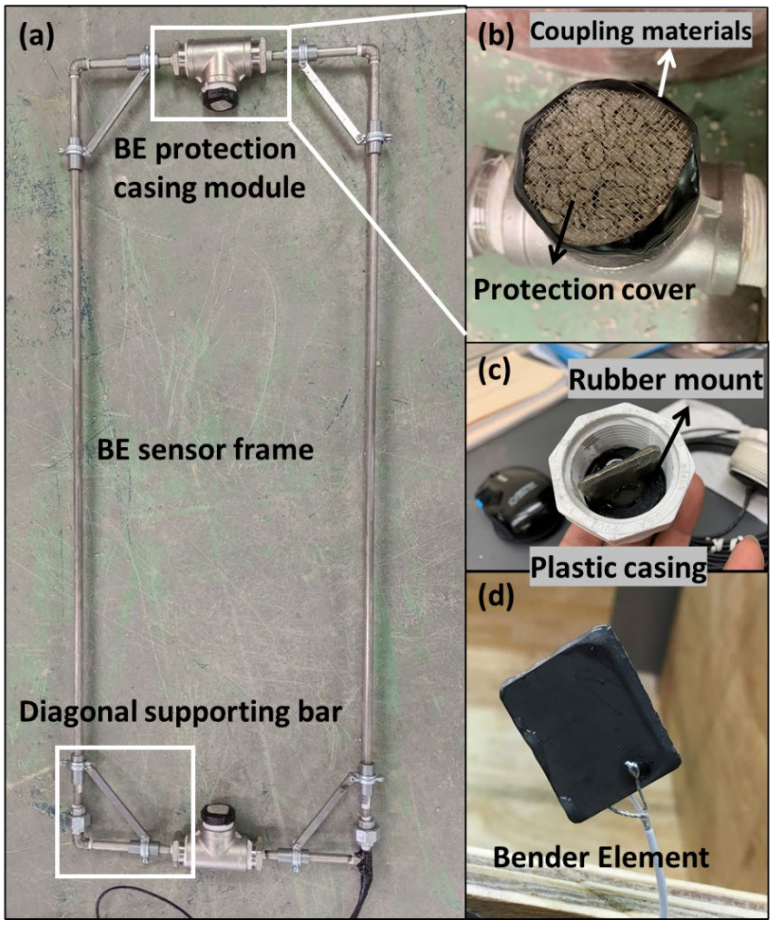

Figure 3. Bender Element Field Sensor: (a) Photo of the BE Field Sensor, (b) BE Protection Casing Module Filled with Coupling Materials, (c) a Plastic Casing with a Rubber Mount and a BE Inside, and (d) a BE Installed in the Casing Module

2.1.2 Optimizing Coaxial Cable

The original design of BE field sensor, which was developed for roadway application, used an RG-174 cable (Kang et al., 2021). RG-174 coaxial cable is constructed with a 0.11-in. jacket made of polyvinyl chloride (PVC), has a shield count of 1, a maximum frequency of 1.0 GHz, and an attenuation of 32 dB. The cable has an outer stranded conductor shield to prevent external interference and crosstalk between adjacent coaxial cables. While this cable has shielding, the thickness of the cable is not suitable for the field installation, considering the operation system of NAPTV, which simulates aircraft loadings and requires high-voltage electricity to operate. Thus, there was a need for better shielding capability of the coaxial cable for the BE field sensor to prevent electrical interference.

To eliminate the electric interference issues, an LMR-195 coaxial cable was selected. The cable is constructed with a 0.195-in. jacket made of polyethylene (PE), 77% thicker than the RG-174 cable, and designed for outdoor use. LMR-195 has a shield count of 2, which is double the number of RG-174 shields, and a radio frequency (RF) shielding of 90 dB. The maximum frequency for this cable is 6 GHz. LMR-195 has an attenuation of 11.8 dB at 1 GHz. Table 1 summarizes the properties of the two coaxial cables.

Table 1. Comparison of Properties of Coaxial Cables

Name	**RG-174**	**LMR-195**
Flex Type	Flexible	Flexible
Impedance	50 Ohm	50 Ohm
Dielectric Type	PE	PE
Velocity of Propagation	66%	80%
Jacket Diameter	0.11 in.	0.195 in.
Jacket Material	PVC	PE
Number of Shields	1	2
Attenuation at 1 GHz.	32 dB	11.8 dB
Power, Maximum at 1 GHz.	17 Watts	90 dB
Frequency, Maximum	1 GHz	6 GHz
Max. Operating Temperature	80 °C	85 °C
Center Conductor Type	Stranded	Solid
Inner Conductor, Number of Strands	7	1

2.1.3 Improving BE Plate Design

BEs consist of two layers of piezoceramic plates bonded to a thin metal shim sandwiched in the middle. The original BE field sensor design used the BE as a shear wave transducer, which is protected by epoxy covering. While the coaxial cable used for the BE field sensor had outer metal braid shielding and an additional shield to ensure high-quality signal transmission, the inner metal of the BE plate was not properly protected from outer interference since the edge of the BE plate was exposed without shielding. Although the BE plates are covered with epoxy and surrounded by coupling materials, this exposed part could be a source of noise considering the NAPTV's high-voltage operation needs.

To minimize the possibility of outer electrical interference, silver conductive paint was used to provide protection. The paint was applied on the epoxy covering the BEs, and then BEs were covered again with epoxy to protect the silver conductive paint. This paint was connected to the outer shielding conductor of the coaxial cable, making this layer function as an extended shielding that fully covered the BEs. The paint is a highly concentrated suspension (43% ± 3% silver solids) of specially prepared and tightly controlled, high-purity silver powder combined with an organic suspending and binder system. The product is formulated to produce electrically conductive paths, patterns, or films over nonconductive surfaces. Figure 4 shows the BEs with and without the silver conductive paint application.

(a) (b)

Figure 4. Bender Element Plates during Manufacturing (a) with and (b) without Silver Conductive Paint

2.1.4 Measurement System for BE Field Sensors

The BE field sensor system used for measuring shear wave velocity is shown in Figure 5. The measurement system includes a signal generator, a linear amplifier, an oscilloscope, a filter-amplifier, and a computer device. The sinusoidal source signal was generated using a signal generator, and the signal was magnified up to six times by the linear amplifier. The amplified signal delivered to the source BE transducer of the BE field sensor is converted to an elastic wave. The receiver BE transducer collects the elastic wave propagating through the aggregates and converts it to an electrical signal. After the filter-amplifier conditions the signal conditioning of the received signal using the filter-amplifier, the output signal is collected by the oscilloscope. The stacking number of 1,024 was used to average the signal to collect a clear signal with a high magnitude. In addition, the resonant frequency of the aggregates was used as an input signal frequency to collect a clear output signal with a high signal-to-noise ratio (Clayton, 2011).

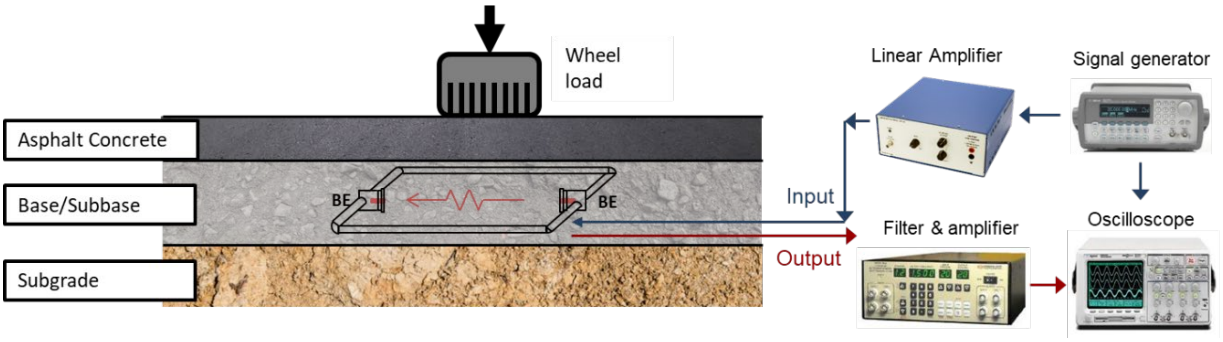

Figure 5. The BE Field Sensor Measurement System

2.1.5 Bender Element Field Sensor Instrumentation

Three BE field sensors (BE 1, BE 2, and BE 3) were installed in the CC9 geosynthetic test area in November 2019. Two of the BE sensors were installed in the geogrid-stabilized P-209MR base layer in test item LFC-3N, and the third was installed in the unstabilized P-209MR base layer of test item LFC-3S (control). Both LFC-3 test items consisted of a 5.0-in. P-401MR asphalt surface with an 8.0-in. P-209MR granular base. Both test items had 29-in.-thick granular subbase layers (P-154MR). Figure 6(b) and (c) show profile views of the two test items where the three BE field sensors were embedded. The P-209MR base was constructed in two equal 4-in. lifts. In the "north" test section, an integrally formed, polypropylene biaxial geogrid with 1.0-in. × 1.3-in. rectangular apertures, was placed at the interface between the subbase and base layers. Two BE field sensors were placed in LFC-3N with geogrids (north section). BE 1 was placed 1.0 in. above the geogrid and BE 3 was installed 4.0 in. above the geogrid. BE 2 was installed 1.0 in. above the bottom of the base layer in the LFC-3S "south" control section. All three sensors were placed under the gear path of the NAPTV.

Figure 7(a) shows the grain-size distribution curve of the P-209 unbound aggregate material used in the CC9 test sections, determined as per American Society for Testing and Materials (ASTM) C136 test procedure (2020). The aggregate base material is classified as A-1-a (stone fragments, gravel, and sand) according to American Association of State Highway and Transportation Officials (AASHTO) soil classification (AASHTO M145-91, 2012), and as SP (poorly graded sand with gravel) according to the Unified Soil Classification System (ASTM D2487-17, 2020). The D_{50} size corresponding to 50% passing in a gradation chart was 0.15 in. (3.8 mm), the top particle size was 1.0 in. (25 mm), and the fines content corresponding to materials passing the No. 200 sieve size (0.075 mm) was 3%. The maximum dry density from the modified Proctor test (ASTM D1557-07, 2010) was 158.0 lb/ft^3 (or pcf) at an optimum moisture content (OMC) of 6.0%, as shown in Figure 7(b).

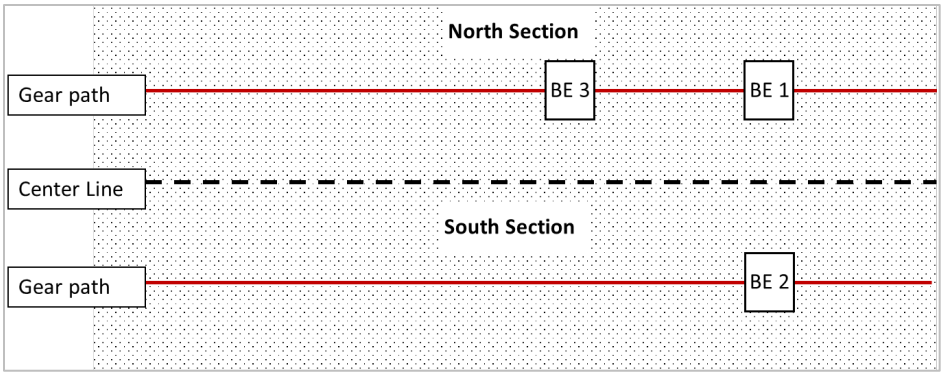

(a)

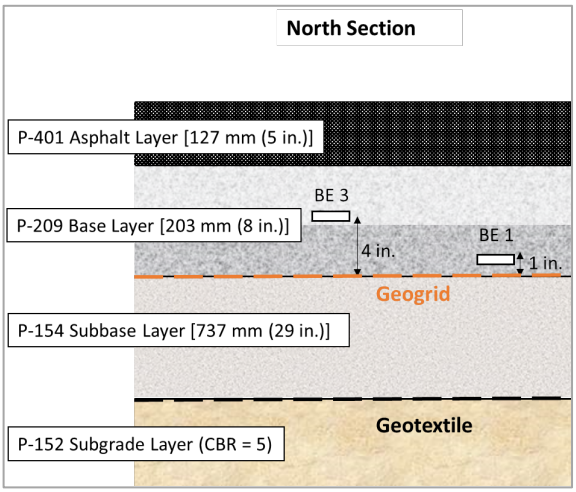

(b)

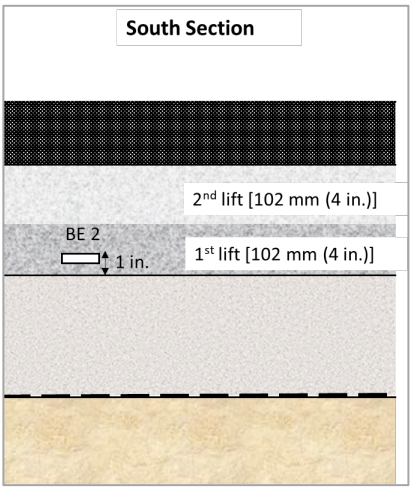

(c)

Figure 6. The CC9 LFC-3 Test Sections showing (a) Plan View, and Profile Views of (b) the BE Sensors Installed in the North Section (with Geogrid) and (c) the BE Sensor Installed in the South Section (with no Geogrid)

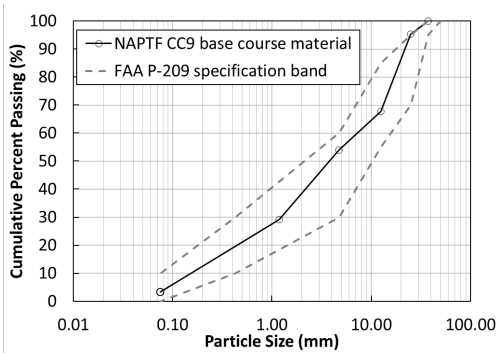

(a)

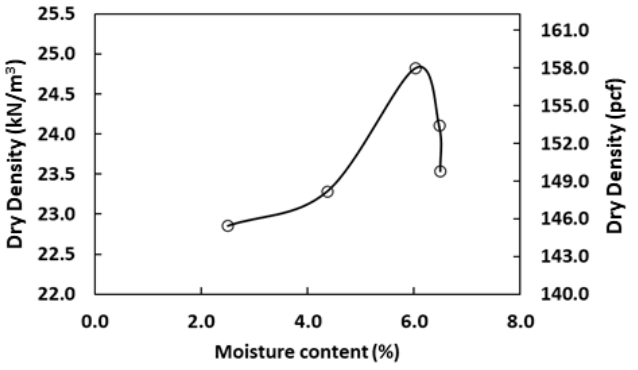

(b)

Figure 7. Aggregate Material Properties for NAPTF CC9: (a) Grain-Size Distribution Curve and (b) Moisture–Density Curve

The base layer was constructed in two 4-in. lifts, as shown in Figure 8(b) and (c). BE 1 and BE 2 were installed after the construction of the first lift and BE 3 was placed after the construction of the second lift. The installation procedure for each BE field sensor was as follows: once the first lift was placed and compacted, the location of the BE field sensor to be installed was marked, and the base course materials were removed to bury the sensor frame, as shown in Figure 8(a) and (b). The trench for the sensor cable was dug to the shoulder of the pavement [see Figure 8(c)]. The aggregate material inside the sensor frame location were kept intact to minimize the disturbance to density and compaction of the materials located between the two BE transducers facing each other [see Figure 8(d)]. The spaces surrounding the sensor frame were filled and compacted to provide a uniform foundation for sensor stability. To ensure full contact between the BE sensors and the base course material, aggregates were gently placed in front of the sensors and compacted by hand tamping. The depth of placement of each BE sensor was carefully measured using a laser level surveying equipment [see Figure 8(e)]. The BE field sensors were then fully covered with the base aggregates and compacted using a vibratory plate compactor [see Figure 8(f)]. The final dry density achieved after proper compaction was 151.3 pcf, which was over 95% of the maximum dry density (158.0 pcf). Figure 9 shows an installed BE field sensor in the aggregate base course and a zoomed-in view of BE 1 field sensor with the geogrid at the bottom.

After installing the BE field sensors, shear wave signals were collected in two stages. Initially, Stage I data were collected after installing BE 1 and BE 2 in the first lift of the P-209MR base layer. Shear wave velocity data were collected before the final compaction with a roller compactor; therefore, the density of the first lift was relatively low (approximately 120 pcf). Figure 9(a) and (b) show the shear wave signals from BE 1 and BE 2, respectively, before placing the second lift and compacting with a vibratory roller. The red arrows indicate the first arrival time of the shear waves. Stage II data collection was performed after the placement and compaction of the second lift and the installation of BE 3 in the second lift. Figure 9(c), (d), and (e) show the shear wave signals from BE 1, BE 2, and BE 3, respectively. Shear wave velocity can be calculated as follows:

$$V_S = \frac{L}{t_{tip-tip}} \tag{1}$$

where $t_{tip\text{-}tip}$ is the first arrival time, and L is the distance between the two BE sensors.

(a) (b)

(c) (d)

(e) (f)

Figure 8. Photographs of BE Field Sensor Installation at NAPTF CC9 showing (a) Marking Sensor Location, (b) Removing Constructed Aggregates, (c) Preparing the Trench for Cables, (d) Placing BE Sensor, (e) Measuring the Placement Depth, and (f) Preliminary Compaction using a Plate

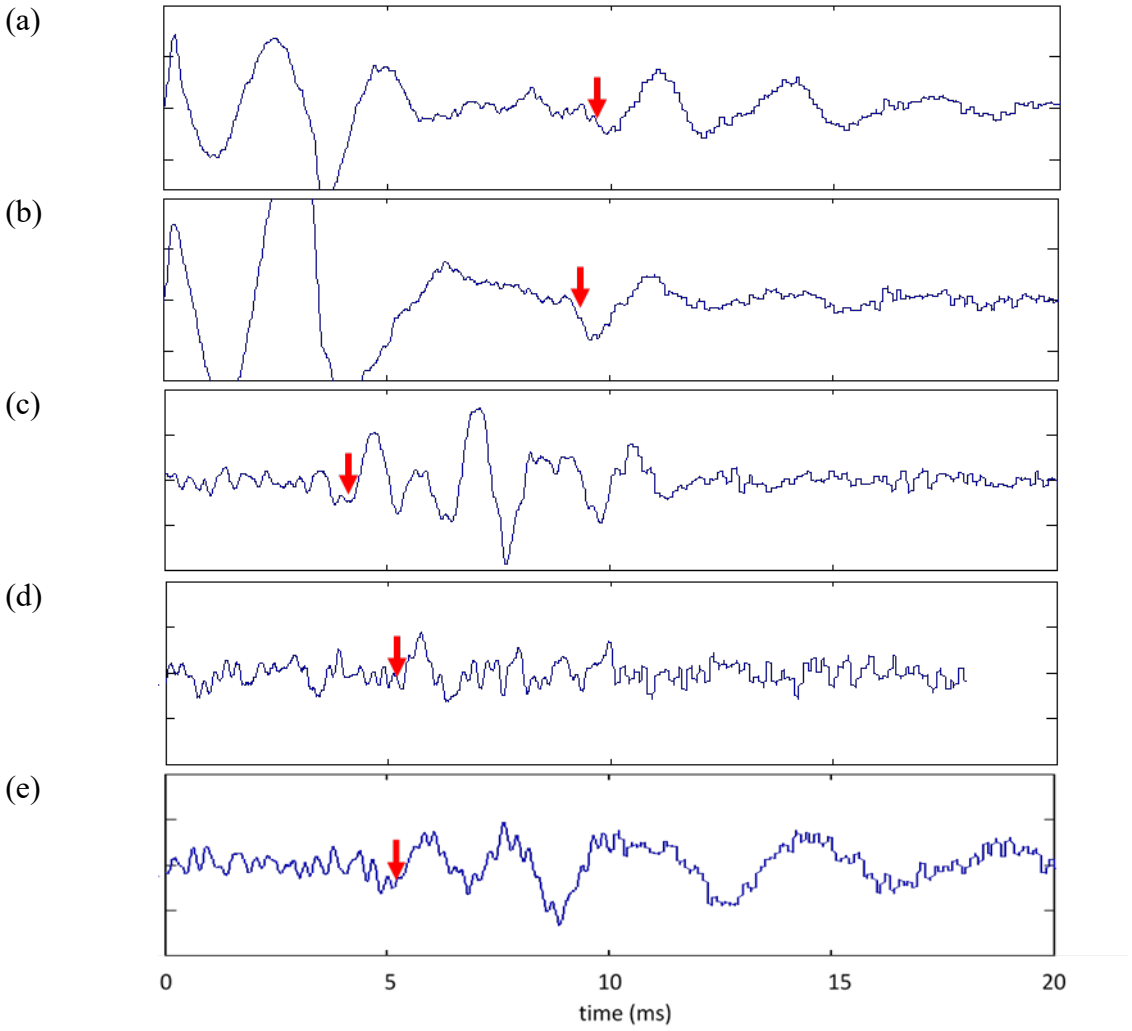

Figure 9. Shear Wave Signals for Stage I (a) BE 1 and (b) BE 2, and Stage II (c) BE 1, (d) BE 2, and (e) BE 3

As shown in Figure 9, the first arrival time of both signals from BE 1 and BE 2 in Stage I are almost identical and do not show any enhanced stiffness from the geogrid. This is likely due to the low density and the relatively small overburden pressure. On the other hand, the first arrival times of the shear wave signals were significantly reduced in Stage II because of the higher density and the higher confinement from the overlying layer. A third measurement was performed after the construction of the hot mix asphalt (HMA) surface layer. Figure 10 shows the shear wave signals collected after finishing the CC9 test section construction. The first arrival times of the shear wave signals further decreased compared to the Stage II measurements because of the higher density, the higher confinement from the overlying layer, and compaction-induced residual that possibly built in the base layer during the compaction of the HMA layer (Kwon & Tutumluer, 2009).

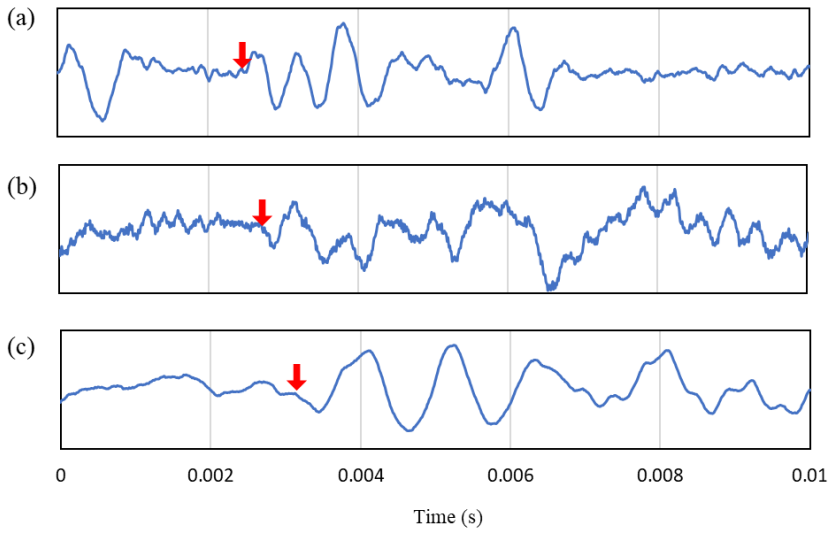

Figure 10. Shear Wave Signals After Construction of HMA for (a) BE 1, (b) BE 2, and (c) BE 3

As a small strain stiffness, shear modulus can be estimated by using Equation 2:

$$G_{max} = \rho V_S^2 \tag{2}$$

where G_{max} is the shear modulus, and ρ is the bulk density of the aggregate material. In addition, the small-strain elastic modulus (E_{max}) of an isotropic material is a function of the shear modulus and Poisson's ratio as expressed in Equation 3:

$$E_{max} = 2G_{max}(1 + \upsilon) \tag{3}$$

Table 2 summarizes the shear wave velocities (V_s), the small-strain elastic moduli, and the resilient moduli of the aggregate base layer from the Stage I and II measurements, during and after constructing the HMA layer. As mentioned above, the moduli from BE 1 and BE 2 at Stage I were comparable regardless of the presence of a geogrid. Considering that the lateral confinement of the aggregate materials is the key to enhancing the geogrid mechanism, it can be concluded that the lateral confinement was not sufficient during Stage I, meaning that the stabilization ability of the geogrid was not fully utilized.

After the construction of the second lift and proper compaction, the modulus dramatically increased for both BE 1 and BE 2. However, the modulus of BE 1, placed in the proximity of a geogrid, was significantly higher than that of BE 2 placed in the control section. This clearly shows the effect of geogrid stabilization in the unbound base layer. A similar trend was observed from the third measurement, after the construction of the surface HMA layer. The highest modulus was measured from BE 1, located near geogrid, whereas BE 2 and BE 3 moduli were lower. The stiffness increase in the base layer after the construction of the overlying layer was notably higher than expected owing to the increased confinement from the 4-in.-thick overlying HMA layer. This can be attributed to the residual stress generated in the base layer during the

construction and compaction of the overlying layers. Kwon & Tutumluer (2009) described the residual stress as locked-in stress in the base and subbase layer during pavement construction, which is due to the large compressive stresses applied to granular layers by compaction equipment. This type of residual stress often can be larger than the stress that aggregate layers might experience during the service life of the pavement (Kwon & Tutumluer 2009). The residual stress built in the aggregate layer during construction/compaction could have resulted in a significant amount of stiffness increase.

Table 2. Shear Wave Velocity, Small-Strain Elastic Modulus, and Resilient Modulus During and After the Construction

Sensor	Testing Stage	Vs [m/s]	E_{max} [ksi]	Notes
BE 1	I	119.2	10.7	
BE 2	I	121.6	11.1	
BE 1	II	287.8	78.6	Near geogrid
BE 2	II	226.9	48.9	No geogrid
BE 3	II	222.6	47.1	4 in. from geogrid
BE 1	III	468.3	208.1	Near geogrid
BE 2	III	427.5	173.5	No geogrid
BE 3	III	364.2	125.9	4 in. from geogrid

2.2 SHEAR WAVE VELOCITY MEASUREMENTS DURING PRE-TRAFFIC TESTS

2.2.1 Test Procedure

2.2.1.1 Pre-Traffic Test

Five stages of shear wave velocity (V_s) measurement tests were conducted using two BE field sensors installed in the unbound aggregate base layer at the north and south sections. Table 3 summarizes the test conditions and timings of each stage. The first test (Test No.1) was conducted after pavement construction was completed. In the pre-traffic testing stage (Test Nos. 2–5), shear wave signals were collected at the north and south sections before applying any vehicle load on the pavement. These data reflect the effect of compaction and construction, and they can be used to compare with the test results to see the effect of vehicle loadings.

Table 3. Loading Test Conditions

Test No.	Test Name	Date of Testing	Wheel Configuration	Load Level [kips]	Position of Module (offset) [ft]	Test Detail
1	Before loading	Nov 2019	N/A	N/A	N/A	V_s measurement before loading
2	Static load test 1	Oct 2020	One dual-wheel module	5, 10, 15, 20	0	V_s measurement with static loading
3	Slow-roll test	Nov 2020	Three dual-wheel modules	12, 24, 36	4.5, 2.25, 0, -2.25, -4.5	V_s measurement after moving wheel loading at 5 offset locations
4	Proof-roll test	Feb 2021	One dual-wheel module	20	4.34 to -12.32, at intervals of 0.833 ft	V_s measurement before/after 42 passes of moving wheel loading
5	Static load test 2	Mar 2021	One dual-wheel module	5, 10, 15, 20	0	V_s measurement with static loading
6	Traffic test	Mar 2021~ Ongoing as of Sep 2023	Three Dual-wheel module	58	Nine wander positions	V_s measurement after 1 or 3 full wander pattern sequences

*1 kip = 1,000 lb = 4.45 kN, 1 ft = 0.3 m

2.2.1.2 Static Load Test

Two static load tests were performed in the test sequence. The first, referred to as Test No. 2, was conducted after Test 1 to investigate the effect of static load on the airport pavement base layer behavior. The unbound aggregate base material is a coarse-grained material that has a stress-hardening behavior (Garg & Thompson, 1997). Stiffness measurement at different stress states is one of the properly established functions of the BE field sensor. During Test No. 2, the dual-wheel single-axle gear configuration (D) module of the NAPTV was located on the surface of the pavement, aligning the gear centerline above the BE field sensor location as shown in Figure 4(a) and (b). The dual wheel spacing used in gear configuration was 54 in., and the tire pressure applied in this experiment was 255 psi. Four stages of static gear loads, from 5 kips to 20 kips at each wheel, in increments of 5 kips, were applied on the pavement. Shear wave signals were collected at each stage of loading using both BE 1 and BE 2 sensors.

The second static load test, referred to as Test No. 5, was performed after finishing dynamic loading tests (Test Nos. 3 and 4), following the same procedure as Test No. 2 (see Table 3).

2.2.1.3 Slow-Roll Response Test

To study the effect of slow-roll dynamic load and the vehicle wander pattern, Test No. 3, referred to as the slow-roll response test, was conducted. The dual-wheel tridem-axle gear configuration (3D) module of the NAPTV was used to apply the dynamic gear loading to the test section. The traffic loading was applied with a travel speed of 0.5 mph, which represents slow-moving aircraft loading. Figure 11(c) shows the gear path distribution across the test section during Test No. 3. The five passes of traffic loading were applied at the five offset locations arranged in equally spaced wander positions at 27-in. intervals, five traveling east and five traveling west [see Figure 11(c)]. The same traffic sequence was applied at the north and south sections, and the test was repeated for three load levels: 12, 24, and 36 kips (see Table 3). Shear wave velocities were collected after two passes of traffic loading at each wander position, without any load applied to the pavement while the gear load module was parked outside of the testing pavement sections.

2.2.1.4 Proof-Roll Test

During Test No.4, referred to as the proof-roll test, traffic load was applied on both the north and south sides of CC9 test sections, using a two-wheel single-axle (D) gear at 20 kips per wheel. The proof-roll test wander pattern and track locations are shown in Figure 11(d). Forty-two (42) passes of traffic loading were applied at the 21 offset locations arranged in equally spaced wander positions at 10-in. intervals, 21 traveling east and 21 traveling west [see Figure 11(d) and Table 3]. Shear wave velocities were collected before and after Test No. 4 using both BE 1 and BE 2 sensors.

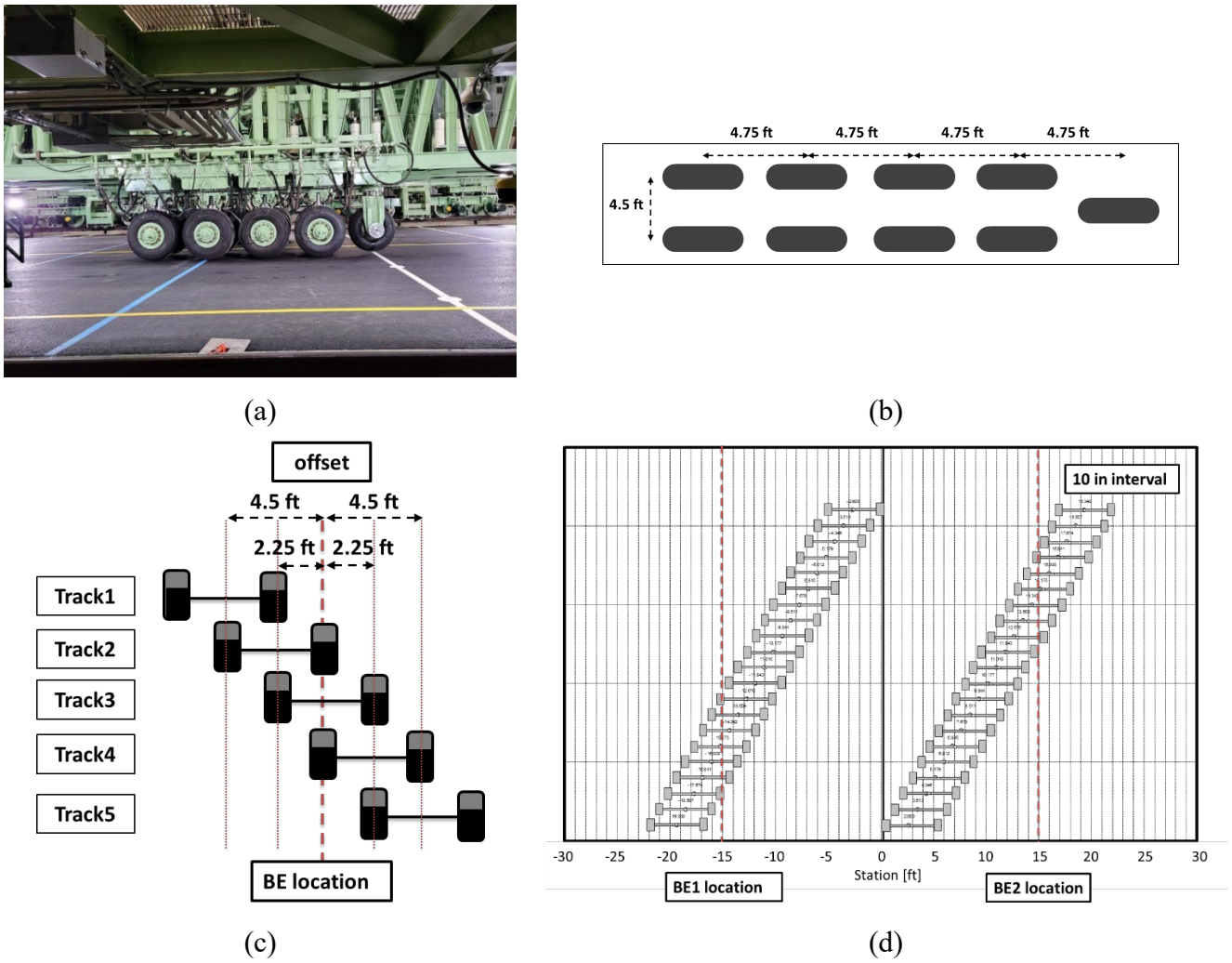

Figure 11. Load Module and Vehicle Loading Sequence for the NAPTV showing (a) the NAPTV Load Module, (b) the NAPTV Load Module Configuration, (c) the Slow-Roll Sequence, and (d) the Proof-Roll Sequence

2.2.2 RESULTS AND DISCUSSION

2.2.2.1 Effect of Static Wheel Load

The typical shear wave signals measured during Test No. 5 static load test using BE 1 and BE 2 sensors are presented in Figure 12. The shear wave velocity was estimated using the distance between the source and receiver BE transducer tips and the first arrival time of the signal using Equation 1. Shear wave velocity is a function of the stiffness of the medium, as shown in Equation 2. Thus, shear wave velocity represents the small-strain stiffness of the aggregate layer.

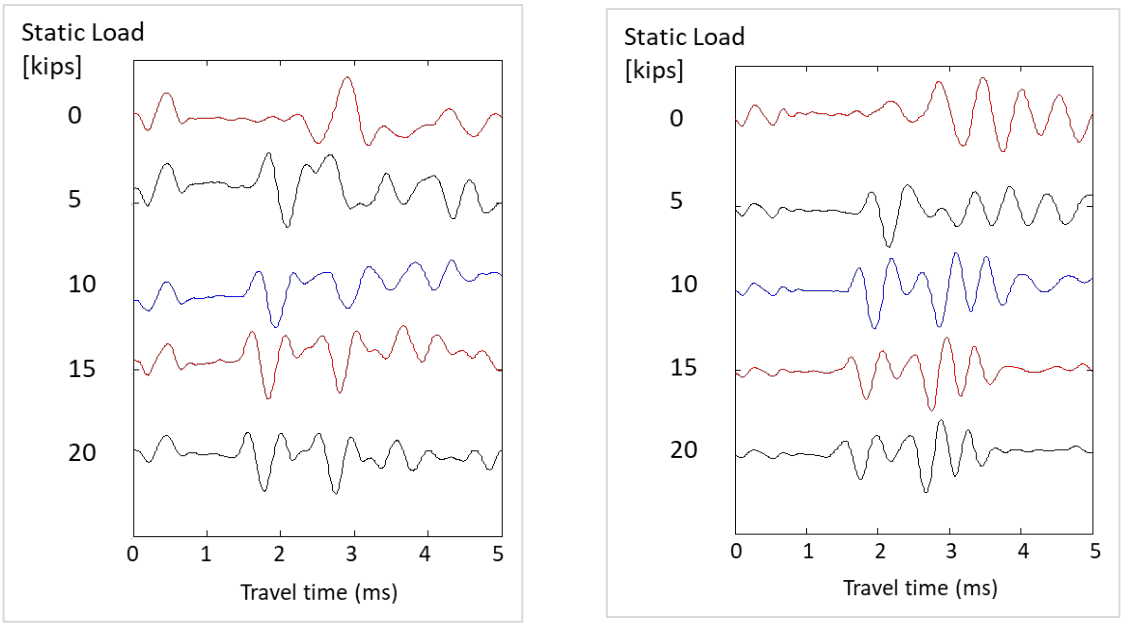

(a) (b)

Figure 12. Typical Shear Wave Signals during Test No. 5 at the (a) North and (b) South Sections

Static wheel load tests were conducted before and after load application (Test Nos. 2 and 5, respectively). Figure 13 shows the variations in shear wave velocities with static loading during the two tests. The V_s increased with the higher static loading applied on the pavement. V_s is a function of confining pressure as expressed in Equation 4.

$$V_S = \left(\frac{G_{max}}{\rho}\right)^{0.5} = a\sigma_c^b \tag{4}$$

where σ_c is applied confining pressure and a and b are regression coefficients that can be obtained from laboratory testing. Because the confining pressure applied at the BE field sensor location increases with increasing the static wheel load, V_s can be expressed as a function of the static load as follows:

$$V_S = \alpha P^{\beta} \tag{5}$$

where V_S is a shear wave velocity [m/s (mph)], P is the static load per wheel [kips (kN)], and α and β are model parameters determined from regression analysis.

The regression models from the static load test follow a power function trend line, as shown in Figure 13. The model parameters for each test are summarized in Table 4. From previous experimental research studies, it is well-known that the modulus of the aggregate material is stress-dependent (Rada & Witczak, 1981; Santamarina, 2001). The test results from these four tests fit the power function regression model with a high coefficient of determination (R^2) exceeding 0.97. For the same magnitude of the static loading condition, V_s collected from Test No. 5 are higher than those from Test No. 2. Note that after Test No. 2 and before Test No. 5 was

conducted, multiple passes of gear/wheel loads as high as 36 kips were applied to the pavement during Test Nos. 3 and 4. This is analogous to the initial load repetitions applied as a conditioning stage in repeated load triaxial testing to stabilize the specimen by rearranging the aggregate particles (Byun et al., 2020; Kang et al., 2020). Considering the test sequence, multiple repetitions of vehicle traffic loading rearranged the aggregate particles and increased the stiffness of the base layer.

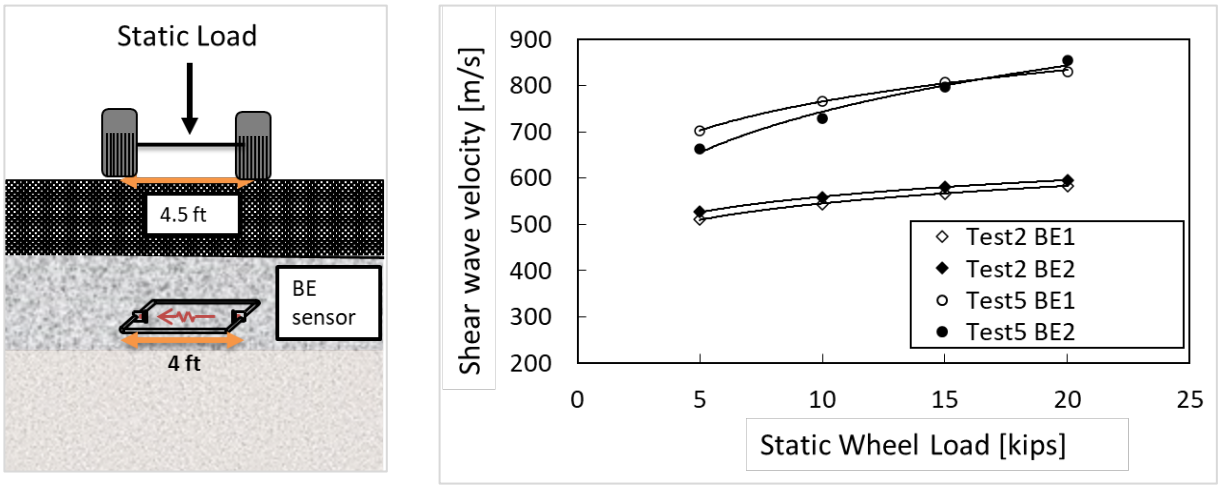

(a) (b)

Figure 13. Shear Wave Velocity (V_s) during Static Loading showing (a) Position of the Sensor and the Loading Modulus during Test Nos. 2 and 5 and (b) Variations in V_s with Static Wheel Loading

Table 4. Model Parameters for Determining Shear Wave Velocity from Static Wheel Load

Test No.	BE Sensor	Model Parameters		
		α	β	R^2
2	BE 1	436.47	0.0968	0.9986
2	BE 2	455.94	0.0894	0.9996
5	BE 1	576.89	0.1230	0.9979
5	BE 2	489.18	0.1819	0.9796

2.2.2.2 Effect of Moving Wheel Load and Vehicle Wander

The slow-roll response test (Test No. 3) was conducted using a 3D gear module with a travel speed of 0.5 mph at three different load levels. The traffic-loading offset locations and the sequence of the loading are shown in Figure 11(c). Figure 14(a) and (b) shows the shear wave signals collected after two gear passes at each offset location. Note that two signals are missing in Figure 14(a) at offset 0 and 2.25 ft after 24 kips passes (i.e., Run Nos. 8 and 9), due to excessive signal noises. Shear wave signals clearly show a variation in shear wave velocities, which are a function of stiffness of material, after loadings at different offset locations.

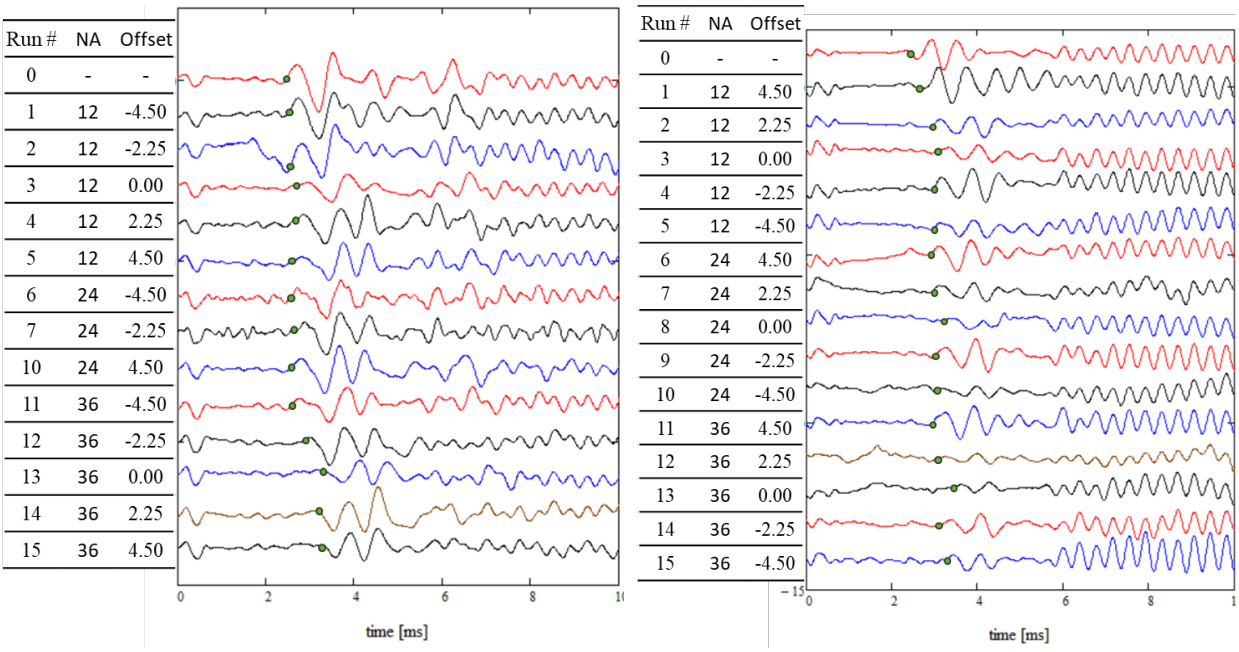

(a) (b)

Figure 14. Shear Wave Signals Collected during Slow-Roll Test from (a) BE 1 and (b) BE 2

Figure 15 shows the variations in V_s measured using BE field sensors during slow-roll testing, Test No. 3. The dashed horizontal line indicates the V_s before the first gear pass. For both BE 1 and BE 2, the V_s decreased after the first pass of the traffic loading. The decrease was the highest at offset 3 when the vehicle gear load was applied at the sensor location. However, the velocity recovered after the gear passes at offset 4.

From a previous research study, during the analyses of the NAPTF multi-depth deflectometer (MDD) data, Donovan & Tutumluer (2008) observed an "anti-shakedown" effect. This phenomenon occurs when the downward permanent deformation, which is caused by one wheel pass of heavy gear, is canceled by the upward dilative deformation, which results when the pass of the gear is transversely offset by wander (Donovan et al., 2016; Donovan, 2009). This interaction indicated a shuffling or rearrangement of the aggregate particles, which reduced the strength of the unbound layer. More recently from the full-scale tests at the CC5 experiment with multi-depth deflectometer measurements at NAPTF, heaving of the pavement system and individual layers after the heavy gear traffic loading was observed under the centerline of the dual-wheel gear, which is at offset 3 in this experiment (Sarker, 2020; Sarker & Tutumluer, 2018). Additionally in this experiment, considerable heave was reported when both wheels of the loading module passed the outer offset location from the sensor location, which is offset 1 and offset 5 locations. On the other hand, the downward residual deflection was the maximum under the wheel location, i.e., offset 2 and offset 4.

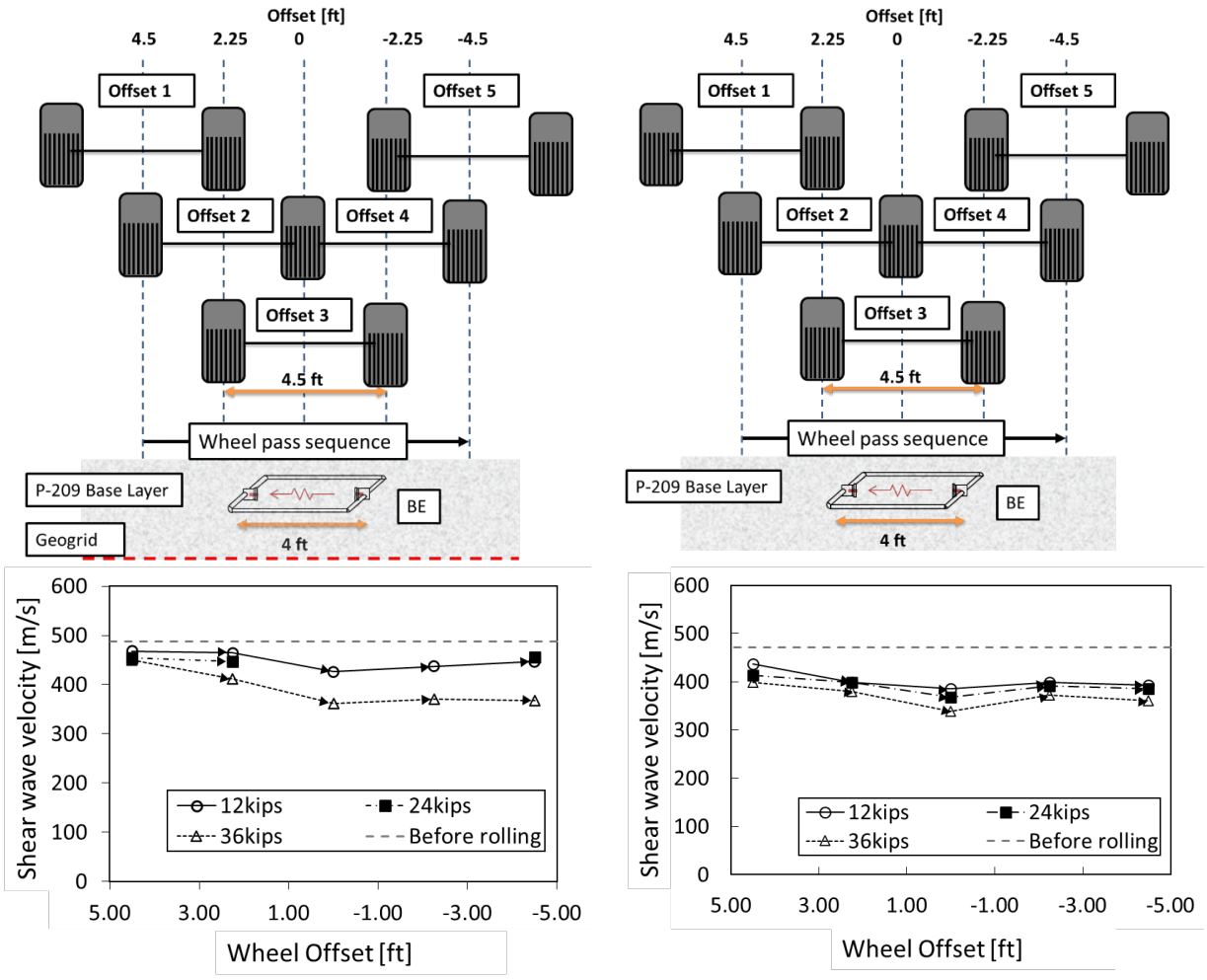

(a) BE 1 with geogrid

(b) BE 2 control

Figure 15. Variations in Shear Wave Velocity during Slow-Roll Testing shown with Dynamic Wheel Load Location for (a) BE 1 after Each Wheel Pass and (b) BE 2 after Each Wheel Pass

Figure 16 shows the pavement behavior under the dual-wheel dynamic load. High vertical stress under the wheel causes downward deflection (offsets 2 and 4), while high horizontal stress under a certain distance from the wheel load results in an upward heave (offsets 1, 3, and 5). At offset 3, V_s was the lowest for both the north and south sections due to the dilation of the aggregates. However, the resilient modulus recovered after traffic loading at offset 4 due to the compression. As expected, the change in V_s was the highest after the highest traffic load of 36 kips was applied. Therefore, stiffness estimated via V_s data collected throughout the slow-roll response test is in accordance with previous research findings.

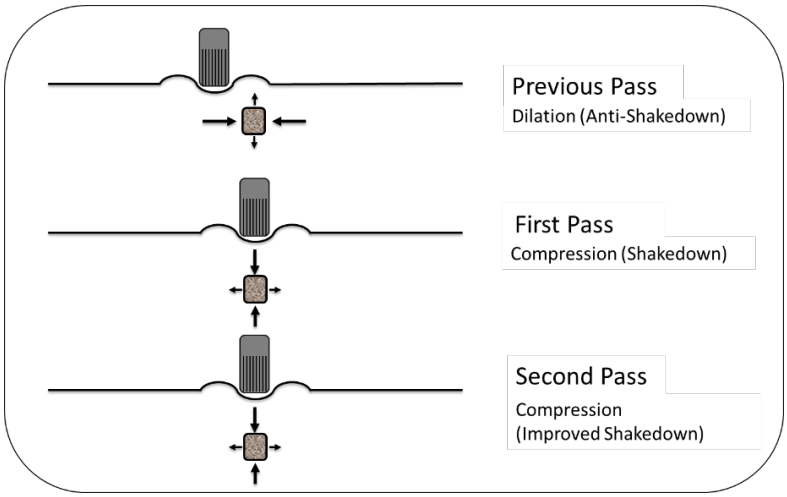

Figure 16. The Effect of Consecutive Wheel Passes on an Unbound Aggregate Base Considering Offset Load Wander Applied at the Previous Pass (modified from Donovan, 2009)

The proof-roll test (Test No. 4) was conducted after finishing Test No. 3, and the V_s were collected before and after the test. Figure 17 shows the comparison between V_s measured before and after moving wheel load tests. From the "After Test 3" data, the lowest V_s were selected. The moving wheel load with wander pattern caused a loss of stiffness in the unbound aggregate layer due to particle rearrangement or shuffling. The change in V_s was much lower for Test No. 4, which used the dual-wheel single-axle (D) configuration with 20 kips load per wheel, while the dual-tridem (3D) gear with 36 kips loading passes was applied during Test No. 3. Thus, the previous compaction and consolidation at the higher load level reduced the effect of proof-rolling.

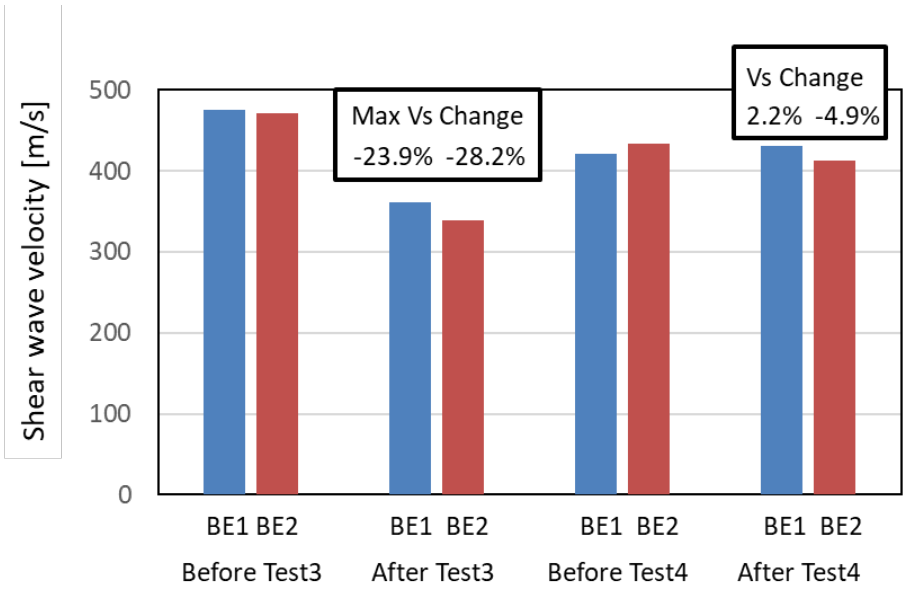

Figure 17. Effect of Moving Wheel Load on Shear Wave Velocity (V_s)

2.2.2.3 Effect of Geogrid Stabilization

The north section of the LFC-3 test section with BE 1 was a geogrid-stabilized section, while the south section with BE 2 was an unstabilized control section. Table 5 summarizes the V_s at each test stage with and without geogrid, and the difference between V_s from BE 1 and BE 2. From Test No. 1 after pavement construction, V_s at the geogrid-stabilized section was 9.5% higher than that measured in the unstabilized section. In addition, the effect of geogrid-stabilization is well indicated after the moving wheel loading, as highlighted in Figure 17 and Table 5. The reduction in V_s after the moving wheel loading in the unstabilized section was higher than that of the geogrid-stabilized section. Thus, it can be concluded that the geogrid-aggregated interlocking generated in the geogrid-stabilized section reduced the rearrangement and movement of the aggregates during moving wheel loading. While the effect of geogrid stabilization was apparent after the moving wheel load, the effect was not clear during the static load tests as shown in Figure 13. This might indicate that the geogrid stabilization effect could decrease when the layer stiffness reaches a certain high-level owing to the high confining pressure applied.

Table 5. Effect of Geogrid Stabilization Throughout the NAPTF Pre-Trafficking Tests

	Test No. 1 V_s [m/s]	**Before Test No. 3 V_s [m/s]**	**After Test No. 3 V_s [m/s]**	**Before Test No. 4 V_s [m/s]**	**After Test No. 4 V_s [m/s]**
BE 1	468.25	475.81	361.96	421.43	430.66
BE 2	427.54	472	339.08	433.82	412.59
Percent Difference (%)	9.52	0.81	6.75	-2.86	4.38

2.3 SHEAR WAVE VELOCITY MEASUREMENTS DURING TRAFFIC TESTS

As of September 2023, a total of 40,128 passes were applied to the CC9 LFC-3 test sections. While BE field sensor data were collected throughout the testing, the quality of BE field sensor data degraded after 10,494 passes, i.e., after 159 wander patterns. This section focuses on the results collected from test item LFC-3 during the first 10,494 vehicle passes.

2.3.1 Laboratory Tests to Convert BE Modulus to Resilient Modulus

While BE field sensors measure the shear wave velocities that depend on a material stiffness in a small-strain range, the resilient modulus is characterized in a larger-strain range due to pulsed vehicular loads realistically applying large deviator stress excursions. Considering the modulus degradation with increasing strain levels, the correlation between small- and large-strain moduli first needs to be established for conversion (Kang, Wang, Qambia, & Tutumluer, 2022).

The P-209 aggregate materials from the CC9 test section were sampled to conduct laboratory resilient modulus tests. Repeated load triaxial testing was performed according to AASHTO T307-99 (2003), resilient modulus test procedure for stress-hardening materials. Figure 18(a) shows a schematic drawing of the laboratory test setup. A cylindrical specimen with a diameter of 150 mm (5.9 in.) and a height of 150 mm (5.9 in.) was prepared, and the testing was performed using the UI-FastCell, which is an advanced triaxial testing device allowing dynamic stresses to be applied independently in the vertical and horizontal directions (Tutumluer &

Seyhan, 1999). Following 1,000 load cycles of specimen conditioning at a 15-psi confining pressure and a 15 psi deviatoric stress, 15 stages (100 load cycles per stage) were applied sequentially, covering a bulk stress range of 12 to 100 psi. One load cycle consists of 0.1-second load pulse followed by a 0.9-second rest period [see Figure 18(b)]. The resilient modulus at each stress state was calculated from the applied loads and axial recoverable strains. Meanwhile, the shear waves were measured after the application of 100 load cycles of each stress state, using a BE pair installed at the mid-specimen height.

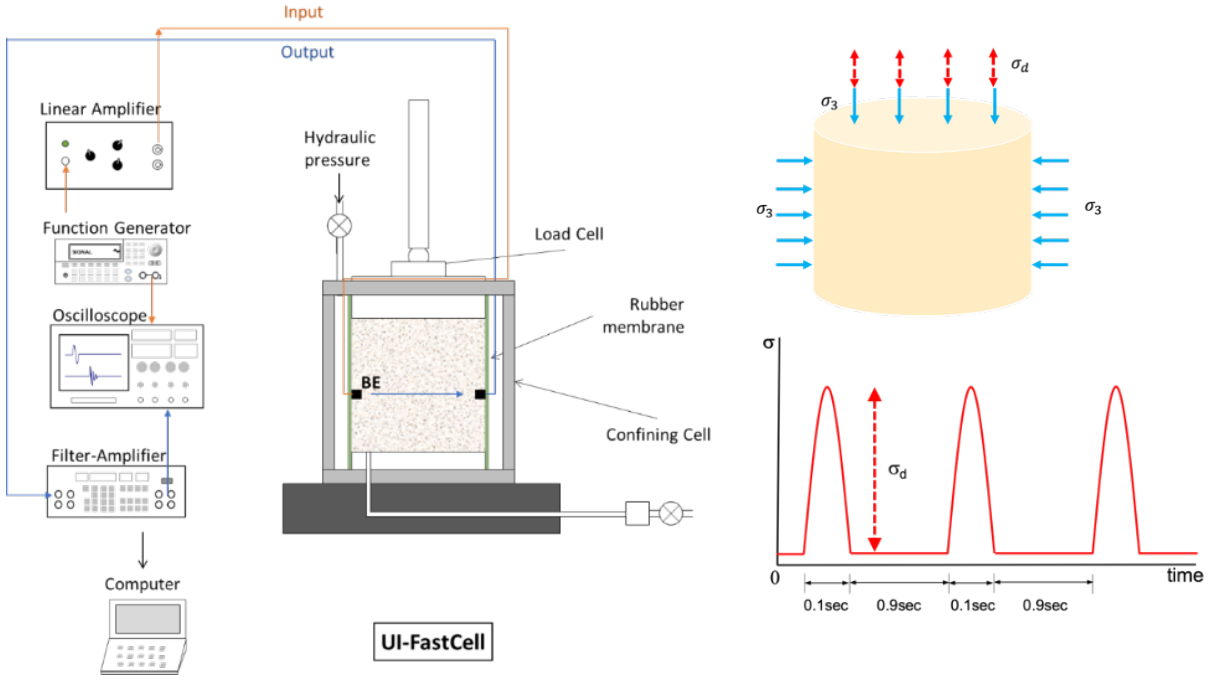

(a) (b)

Figure 18. UI-FastCell (a) Test Configuration and (b) Loading Pulses during Repeated-Load Triaxial Tests

During the repeated-load triaxial testing using the UI-Fastcell, resilient strains and applied stress states were recorded from all 2,500 load cycles. The resilient strain and deviator stress values from the last five cycles of each 100 load repetitions were averaged to calculate the resilient moduli at each stress state. The resilient modulus (M_R) can be calculated using Equation 6:

$$M_R = \frac{\sigma_d}{\varepsilon_r} \tag{6}$$

where σ_d is deviator stress, and ε_r is the recoverable resilient strain.

Figure 19 shows the resilient moduli computed at each stress state from the repeated load triaxial testing. The increase in resilient modulus with increasing bulk stress demonstrates the stress-hardening feature of the P-209 crushed aggregate material. The K-θ bulk stress model for M_R, proposed by Hicks & Monismith (1971), was used to characterize the stress-dependent moduli with a high coefficient of determination.

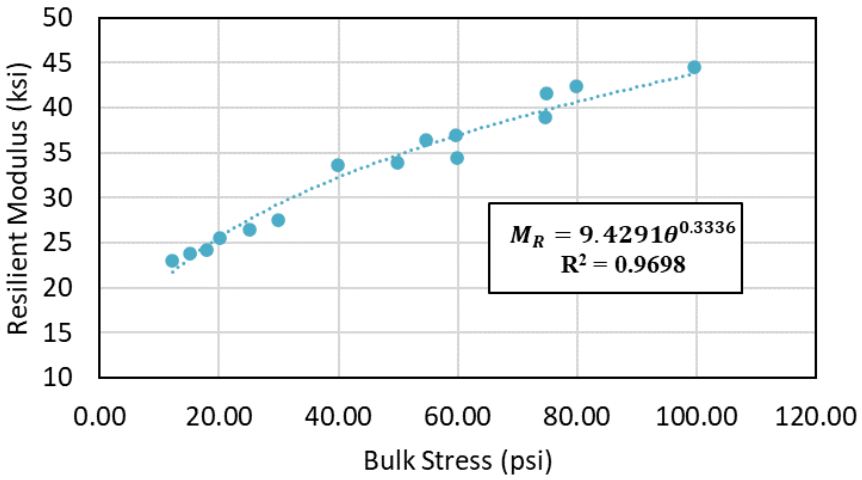

Figure 19. Resilient Modulus (K-θ model) for the P-209 Crushed Aggregate Material

The shear wave signals collected using a pair of BE at the end of each of the 15 applied stress states are presented in Figure 20(a). The first arrival times are presented as green dots on the signals. Shear wave velocities (V_s) were then calculated using Equation 1. Figure 20(b) shows the V_s calculated at the 15 stress states and graphed with the bulk stress. Like the resilient modulus trends shown in Figure 19, the V_s also increased with increasing applied bulk stress.

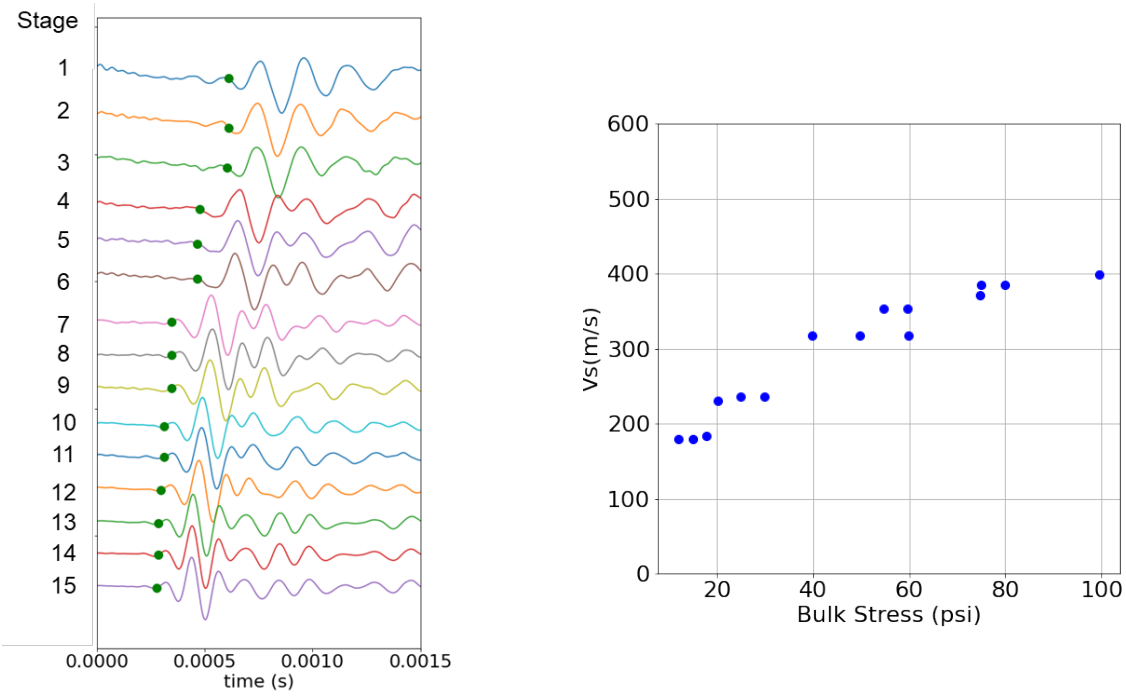

(a) (b)

Figure 20. Bender Element Measurements during Repeated Load Triaxial Test: (a) Shear Wave Signals and (b) Shear Wave Velocities Graphed with Bulk Stress

Small-strain elastic modulus can be derived from the V_s measurements from BE field sensors using Equation 3. A Poisson's ratio of 0.35 was assumed for the granular material in this experiment.

It is well-known that unbound granular materials exhibit modulus degradation with increased strain (Ishibashi & Zhang, 1993; Seed & Idriss, 1970). The correlation between the resilient modulus in the large-strain range and the BE modulus in the small-strain range is presented in Figure 21. The P-209 aggregate base materials indicated a linear relationship between resilient modulus and BE modulus with a coefficient of determination of 0.987, as given in Equation 7.

$$M_R = 0.1802E_{BE} + 18.081 \quad (7)$$

In accordance, the resilient moduli were proportionally lower than the BE moduli, which is expected. Kang, Wang, Qamhia, & Tutumluer (2022) reported the effect of increased confining pressure and that of increased strain to offset each other, resulting in a stable modulus ratio. The correlation established from the laboratory study was then used to assess in situ modulus from BE field sensor measurements at NAPTF CC9 test section.

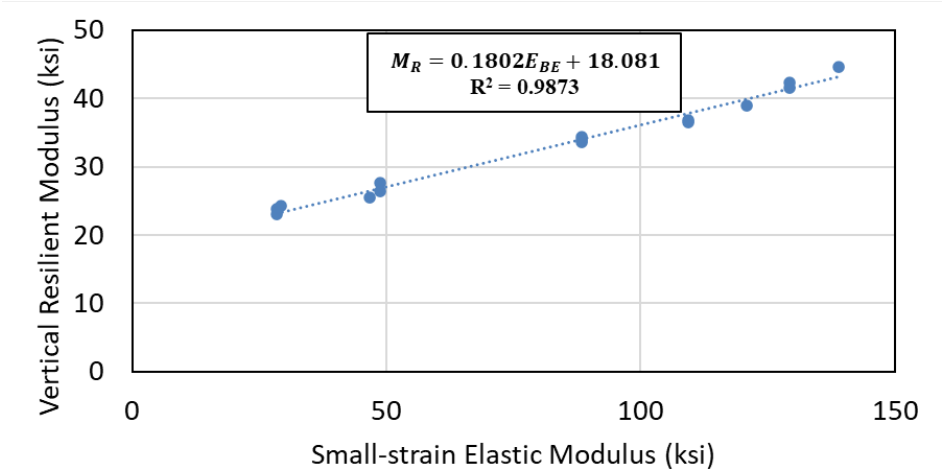

Figure 21. Correlation Between Resilient Modulus and Small-Strain Elastic Modulus

2.3.2 Procedure for NAPTF Traffic Tests

The dual-wheel tridem-axle gear configuration (3D) module of NAPTV applied a dynamic gear loading of 58,000 lb (26 tons) per wheel—a total gear load of 348,000 lb (155 tons)—to the test section during the traffic test. Figure 22(a) shows the gear configuration used in this research. The vehicle simulated a normal distribution of aircraft traffic during testing. Figure 22(b) presents the CC9 gear wander positions applied at different offset distances. The wander pattern consists of 66 vehicle passes arranged in nine wander positions. The red dashed line indicates the sensor location at the centerline of the test section. Note that the offset herein refers to the distance from the centerline of the test section to the centerline of the loading module, which is located midway between the two wheels. Each complete passage of the vehicle to the east counts as one pass, and the complete return to the west counts as a second pass. The complete wander pattern is detailed in Table 6.

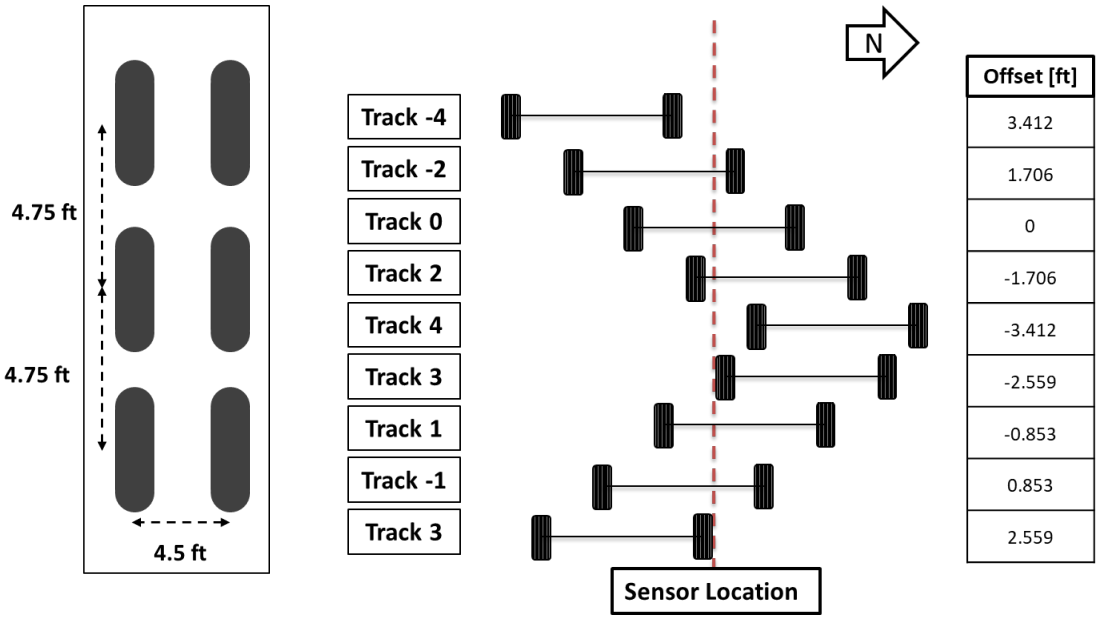

(a) (b)

Figure 22. Loading Procedure for NAPTV Traffic Testing showing (a) Dual-Tridem Load Module Gear Configuration and (b) Wheel Tracks Arranged in Nine Wander Positions Applied to the South Section

Table 6. Details of the Wander Pattern Applied with the NAPTV during Traffic Testing

Pass No.	**1, 2**	**3, 4**	**5, 6**	**7, 8**	**9, 10**	**11, 12**	**13, 14**	**15, 16**	**17, 18**	**19, 20**	**21, 22**
Track No.	-4	-2	0	2	4	3	1	-1	-3	4	-2
Offset (ft)	3.412	1.706	0	-1.706	-3.412	-2.559	-0.853	0.853	2.559	3.412	1.706
Pass No.	**23, 24**	**25, 26**	**27, 28**	**29, 30**	**31, 32**	**33, 34**	**35, 36**	**37, 38**	**39, 40**	**41, 42**	**43, 44**
Track No.	0	2	4	3	1	-1	-3	3	1	-1	-3
Offset (ft)	0	-1.706	-3.412	-2.559	-0.853	0.853	2.559	-2.559	-0.853	0.853	2.559
Pass No.	**45, 46**	**47, 48**	**49, 50**	**51, 52**	**53, 54**	**55, 56**	**57, 58**	**59, 60**	**61, 62**	**63, 64**	**65, 66**
Track No.	-2	0	2	-2	0	2	1	-1	1	-1	0
Offset (ft)	1.706	0	-1.706	1.706	0	-1.706	-0.853	0.853	-0.853	0.853	0

During the traffic tests, dynamic responses from the installed CSs and PCs were also measured and recorded.

To avoid any signal disturbance or excessive noise due to the test vehicle running with high electric voltage, shear wave signals were collected using the BE field sensor after the vehicle completed 66 passes in one wander pattern, without any load applied to the pavement (i.e., while the gear loading module was parked outside of the test sections). The static sensor response from coil sensors without vehicle loading was also collected in between wander patterns.

2.3.3 Airport Pavement Base Layer Stiffness Characteristics using BE Field Sensor

During the initial passes with the dual-wheel tridem-axle (3D) gear, i.e., the primary stabilization stage, shear wave signals were collected frequently. After the primary pavement stabilization stage, shear wave signals were collected at the end of each trafficking day, i.e., after three wander patterns, until the end of the trafficking experiment.

Figure 23 shows the shear wave signals collected from BE 2 at LFC-3S throughout the traffic test. The green dots shown in the figure indicate the first arrival times of the signals. The first arrival time increased dramatically after the initial wheel passes. Unfortunately, sensor measurements from the 6th wander sequence (Pass No. 331) to the 71st wander sequence (Pass No. 4,686) were lost due to issues with data collection.

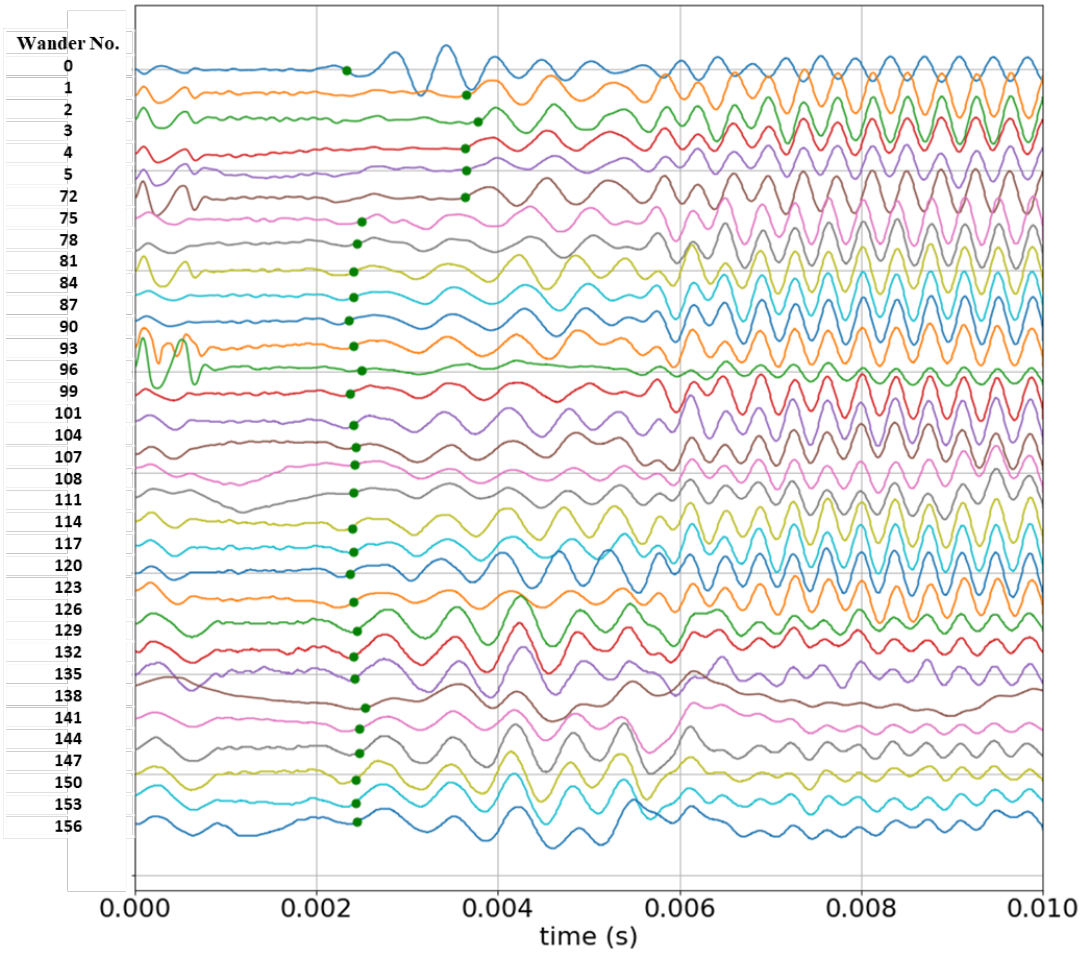

Figure 23. Shear Wave Signals Collected during the Traffic Test at LFC-3S

Figure 24 shows the V_s calculated throughout the traffic test and the M_R values derived using the correlation established from laboratory testing. The modulus values of the unbound aggregate base layer derived from BE measurements were within the typical modulus range of crushed aggregates (AASHTO, 2020; Puppala, 2008; Tutumluer, 2013). Although sensor measurements from the 6th to the 71st wander sequences were lost, the modulus trend throughout the traffic test

is clearly indicated. The modulus of the base layer significantly dropped after the first wander sequence. Such loss was likely due to particle rearrangement, which was the most significant after the initial wander, as reported from the pre-traffic testing of NAPTF CC9 test items (Kang et al., 2022b). After this drop, the modulus gradually recovered up to 10,000 cycles of repeated wheel passes. Note that granular materials exhibit the most deformation accumulation during the initial load pulses in the conditioning stage from repeated load or accelerated pavement testing. The material stabilizes after this conditioning stage (Mishra & Tutumluer, 2012; Qamhia et al., 2017; Thompson & Smith, 1990). The increased modulus trend shows the stabilization of the unbound base layer after the initial conditioning. Note that the BE field sensor data were recorded after every wander sequence when the NAPTV was parked. Thus, it did not show the effect of wander offset locations.

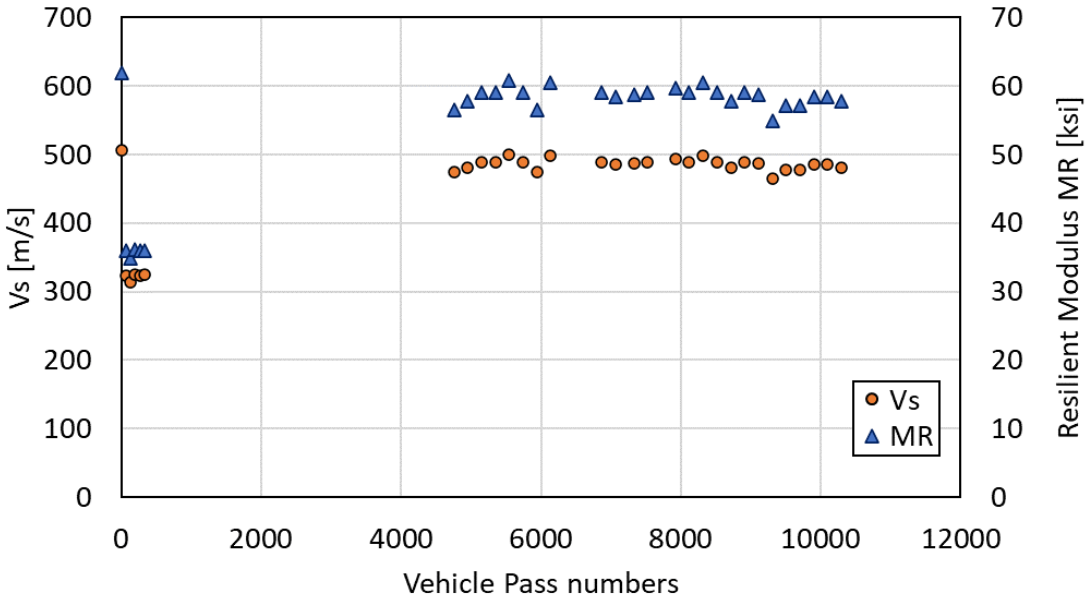

Figure 24. Shear Wave Velocities and Resilient Moduli Obtained from BE Field Sensor during Traffic Test at LFC-3S

Figure 25 shows the shear wave signals collected from BE 1 at LFC-3N throughout the traffic test. Again, the green dots indicate the first arrival time of the signals. Similarly, sensor measurements from the 6th to the 71st wander sequence and from the 87th wander sequence (pass No. 5,545) to the 108th wander sequence (Pass No. 7,128) were lost due to issues with data collection. However, the modulus trend is clear. Like the results of the south section (LFC-3S), the first arrival time increased dramatically after the initial wheel passes. However, unlike the result from the south section, the modulus did not fully recover after trafficking, and it remained relatively constant after the initial loss (see Figure 27).

Figure 26 also shows the V_s throughout the traffic test and the M_R values calculated using the correlation from the laboratory test. The modulus was not fully recovered after the initial loss. This could be attributed to the excessive rutting that was observed at the north section (LFC-3N) during traffic testing. The amount of rutting observed at the LFC-3N section was considerably

higher than that of LFC-3S. After wander sequence 72, the surface rutting measured using a straightedge at the LFC-3N section was 1.77 in., which is 36% higher than that at LFC-3S (1.3 in.). Excessive rutting at LFC-3N section likely deteriorated the base layer, which resulted in a significantly less modulus recovery during traffic testing. Figure 27 shows the comparison between resilient moduli from LFC-3S and LFC-3N. The modulus trend from the two sections shows a notable difference.

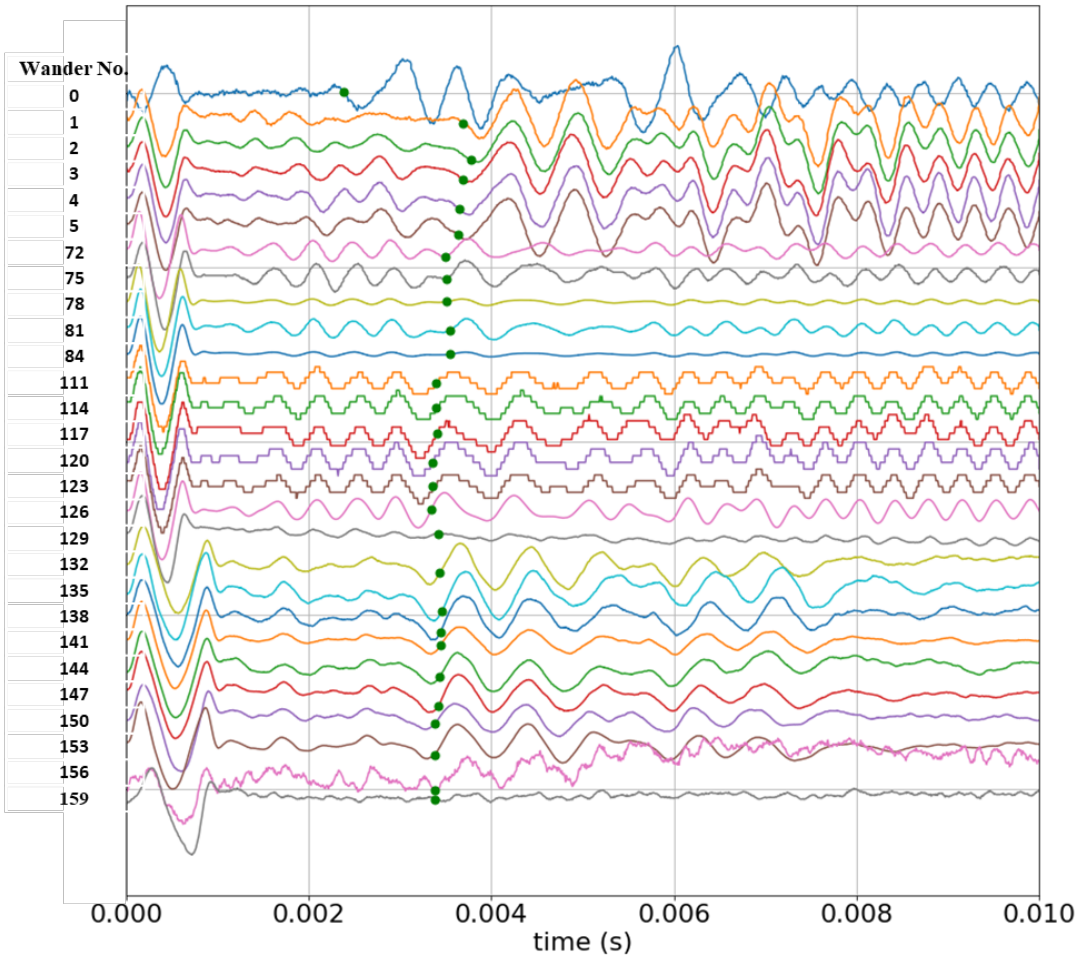

Figure 25. Shear Wave Signals Collected during the Traffic Test at LFC-3N

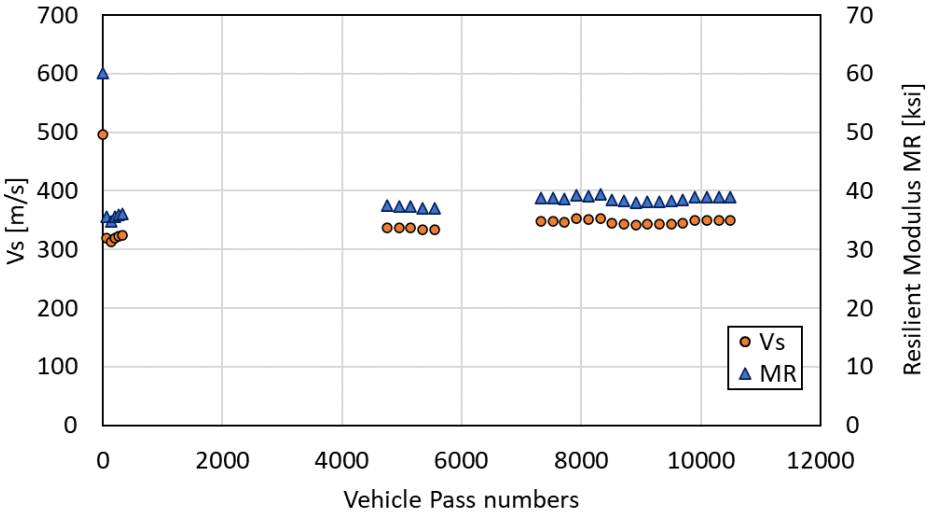

Figure 26. Shear Wave Velocities and Resilient Moduli Obtained from BE Field Sensor during Traffic Test at LFC-3N

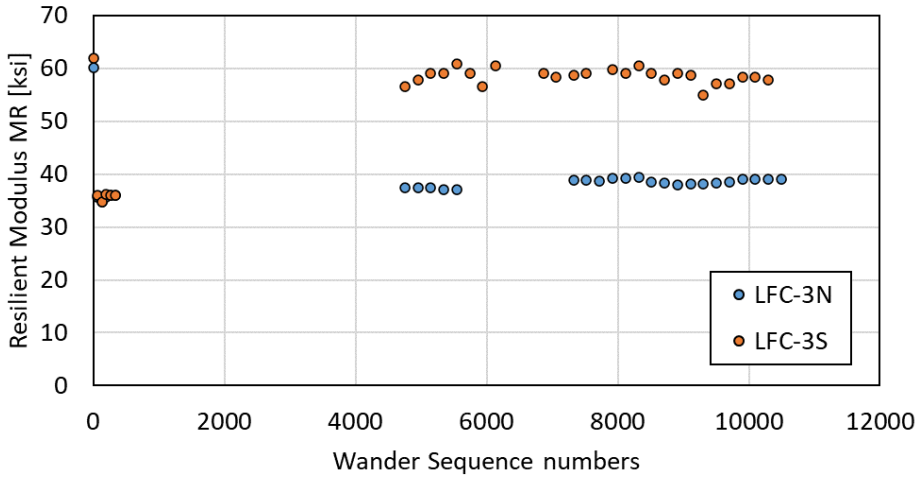

Figure 27. Comparison Between Resilient Moduli from LFC-3S and LFC-3N

2.4 SUMMARY

This section presented research findings regarding the monitoring of stiffness characteristics in airport pavement base layers using a newly developed BE field sensor during the full-scale tests conducted at the CC9 of the FAA NAPTF. Five stages of static and dynamic aircraft gear loadings are conducted as part of the preliminary tests before trafficking the CC9 test sections. Following the pre-traffic tests, the dual-wheel tridem-axle gear configuration loading module of NAPTV applied the dynamic gear loading of 58,000 lb (26.3 tons) per wheel to the test section during the traffic test. The wander pattern of the traffic loading consisted of 66 vehicle passes, arranged in nine wander positions simulating a normal distribution. Dynamic responses of the sensors were measured using coil sensors and the pressure cell, whereas shear wave signals were

collected using BE field sensor after the vehicle completes every 66 passes in one wander pattern of traffic loading. The in situ resilient modulus of the aggregate base layer during the NAPTF traffic test was evaluated.

The resilient moduli estimated via shear wave velocities measured with multiple levels of static loading showed the stress-hardening behavior of the unbound aggregate base layer. From the shear wave velocity measurement after traffic loading passes at various offset locations, a dilative or compressive behavior of the aggregates owing to vehicle wander location was observed.

The moving wheel dynamic tests with certain load wander patterns caused a stiffness loss of the unbound aggregate layer due to particle rearrangement or shuffling. The previously observed "anti-shakedown" effect taking effect in offset loading through the small strain moduli estimated from the shear wave velocity data was highlighted.

The moduli measured from BE field sensor during the traffic test fell within the typical modulus range of unbound aggregates used in pavement base layers. The modulus of the base layer significantly dropped after the first wander sequence of the traffic test due to particle rearrangement or shuffling. The modulus measured at LFC-3S test section showed a gradual recovery of the modulus when loaded up to 10,000-wheel passes owing to the stabilization. It can be concluded that proof rolling is recommended after pavement construction to minimize deflections and modulus/stiffness reductions during the initial traffic loads. On the other hand, modulus measurement from LFC-3N showed minimal modulus recovery after the initial modulus drop, which could be attributed to the excessive rutting that was observed at the north section during traffic test.

3. COIL SENSOR INSTRUMENTATION AND DATA ANALYSES FOR THE P-209MR LAYER

3.1 COIL SENSORS

The inductive coil sensors (CSs) were used as non-contact strain measurement devices. The eight pairs measured a total of 24-in. layer thickness at eight 3-in. deformation increments. A pair of CSs consists of a transmitter and a receiver coil. Any coil can be used as either a transmitter or a receiver. An inductive circuit built with a metal wire surrounding a plastic disk generates a magnetic flux field in the vicinity of the transmitter coil when an alternating current is supplied [see Figure 28(a)]. A receiver coil located in the magnetic flux field generates an output voltage, which is proportional to the distance between two coils through mutual induction (Greenslade et al., 2012). A calibration of the coil sensor was conducted using linear variable differential transformers (LVDTs) installed parallel to the axis of a CS pair, by recording the actual distance and the output voltage [see Figure 28(b)]. The distance between two CSs is expressed by a second-order equation:

$$y = ax^2 + bx + c \tag{8}$$

where x is the output voltage, and y is the distance between the coil sensor pairs. The coefficients a, b, and c are curve-fitting parameters obtained through calibration. The average resolution of

CS is 75 microstrains [2.25×10^{-4} in. (0. 0057 mm)]. To achieve the 3-in. target gap, a digital multimeter was used during installation to obtain the output voltage that corresponded to a 3.1-in. gap. Additional aggregates were backfilled over the upper coil and compacted until the output voltage on a voltmeter was an acceptable indication of the 3 ± 0.1-in. gap. A multiplexor was used in the data acquisition system to route the correct transmitter and receiver coils to the signal conditioning circuit. During each vehicle pass, dynamic pavement deflection responses were monitored using coil sensors.

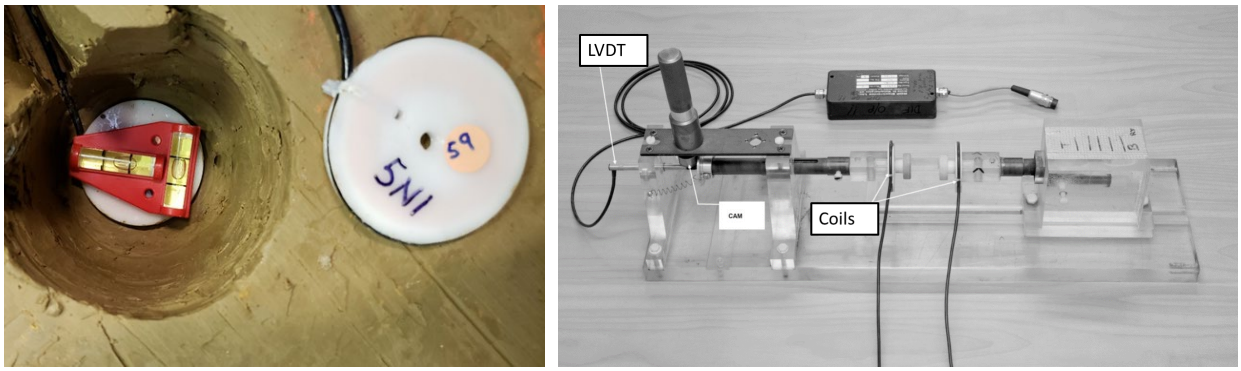

(a) (b)

Figure 28. Embedded CSs showing (a) the CS Pairs and (b) the Calibration Device (modified after Greensdale, 2012)

3.2 FATIGUE MODEL FOR LFS-1

3.2.1 P-209 Layer Deformation at LFS-1S

During the traffic tests, both static and dynamic responses were collected from the CSs. The traffic test on CC9 fatigue model test section was in progress as of September 2023, and this report focuses on the initial 40,000 passes, i.e., the first 606 wander sequences; particularly the static CS responses collected in between each complete wander pattern. In addition, surface rut depth was measured using a 12-ft straightedge in accordance with ASTM E1703 (ASTM E1703/E1703M-10, 2015). The measurement was made after finishing each wander pattern during the first 40 wander pattern studies. The frequency onward was reduced to taking measurements at the end of each day, i.e., typically after three wander patterns.

Figure 29 shows nine CS arrays, which comprise eight CS pairs, installed throughout the full depth of the base layer for both the north and south sections of LFS-1. The arrays of coil sensors measured the output voltage after each complete wander pattern. Voltage readings were converted into the distance between each CS pair. Deformation between each CS pair was quantified by calculating the change in CS pair distance from the initial CS readings before beginning traffic loading. To compute the total permanent deformation of the P-209 layer, the readings from the eight coil sensor pairs were combined for each section.

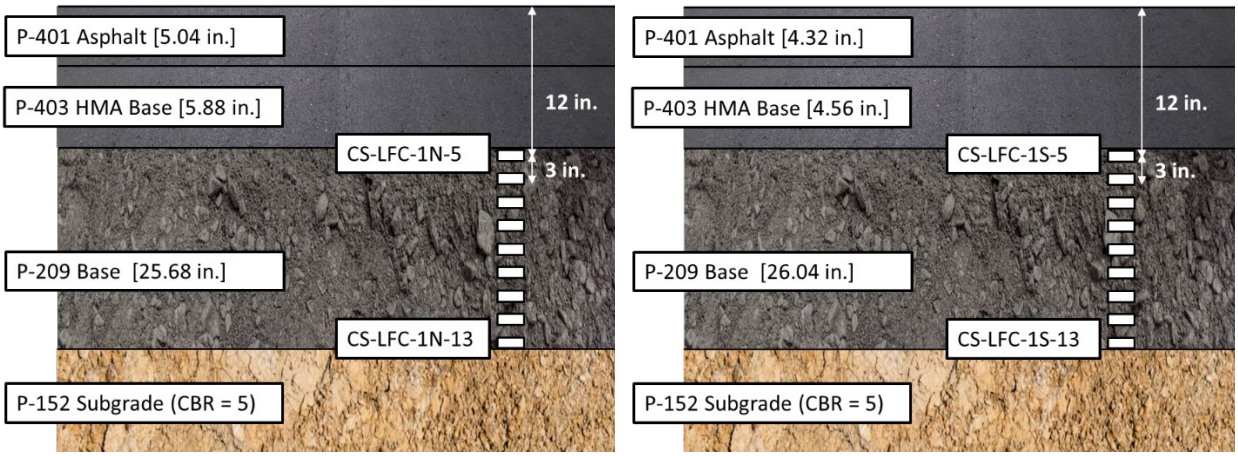

(a) (b)

Figure 29. Cross-Sections of (a) LFS-1N and (b) LFS-1S

Figure 30 shows the total P-209-layer deflection at LFS-1S section throughout the 40,000 vehicle passes, which is estimated through accumulated deformation from eight CS pairs. Pavement deflection increased constantly until approximately pass number 13,000, after which the deflection rate decreased significantly as particle shakedown was mostly completed after primary stabilization. Therefore, from passes 13,000 to approximately 30,000, a steady-state zone was shown as the pavement base layer was stabilized. The deflection rate again increased after the pass number of approximately 30,000. After 26,400 passes, which is in the steady-state zone of the deformation trend, LFS-1S deformed 1.15 in., which is 84.5% of the surface deformation. From previous research on a test section with a similar cross-section and thick P-209 base during the CC1 experiment at NAPTF, the residual deflection of the base layer was approximately 60% of the total residual deflection (Donovan, 2009). The results for CC9 support previous findings that a significant portion of permanent deformation generates in the aggregate base layer. In terms of strain, the vertical strain of the P-209 base layer in LFS-1S was 4.7%.

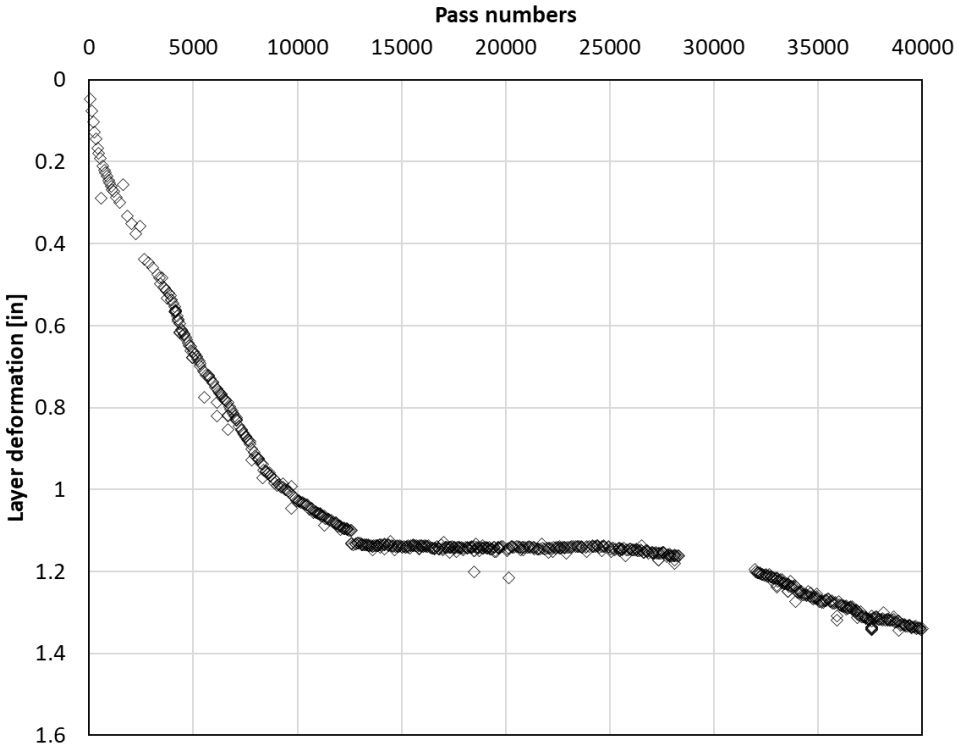

Figure 30. Accumulated Layer Deformation at LFS-1S P-209 Base Layer

One distinctive feature of CS is the capability of measuring the deformation along a short interval of 3 in. Figure 31 shows the distance between coil pairs throughout the 40,000 vehicle passes at LFS-1S section. For example, the data labeled CS-LFS-1S-5/6 indicates the distance between CS 5 and CS 6 in the LFS-1S test section. CS data from pass numbers 28,315 to 31,878 are not included due to a data collection issue. CS data revealed an interesting deformation trend in the thick P-209 base layer with an unexpected critical response location. Most deformation was observed between CS 10 and CS 11, towards the bottom of the rather thick base layer. Figure 32 illustrates the accumulation trends of permanent deformation for each 3-in. interval in the LFS-1S test sections. The contributions of each pair to the permeant deformation for each loading pass are indicated in Figure 32. The maximum deflection of 0.285 in. (8.39 % strain) was generated between CS 10 and CS 11 for LFS-1S, which is between 25- to 28-in. depth from the surface of the pavement.

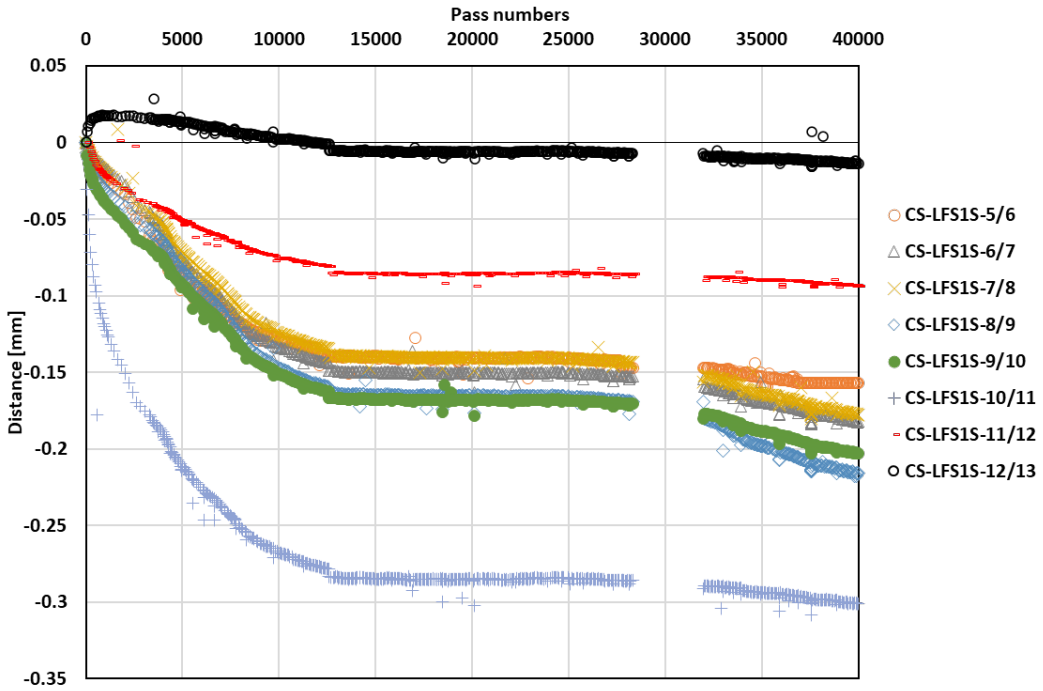

Figure 31. Change in Distance Between Coil Pairs vs Number of Passes at the P-209 Base Layer of LFS-1S

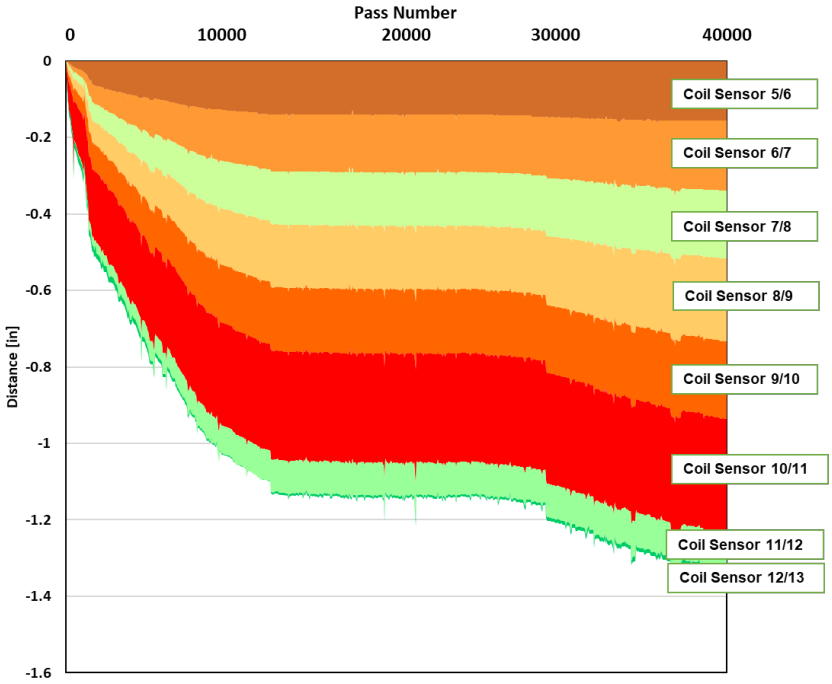

Figure 32. Accumulation Trends of Permanent Deformation for Each 3-in. Interval at P-209 Base Layer of LFS-1S

3.2.2 P-209 Layer Deformation at LFS-1N

Figure 33 presents the total P-209-layer deflection throughout the 40,000 vehicle passes at the LFS-1N section. Like the LFS-1S, pavement deflection increased to approximately pass number 13,000, and a steady-state zone is shown from the pass number of 13,000 to approximately 30,000. After 26,400 passes, the P-209 layer in LFS-1N deformed 0.92 in., which accounts for 75.6% of the total surface deformation. The vertical strain of the P-209 base layer in LFS-1N was 3.8%. LFS-1N deformed less than LFS-1S owing to the thicker HMA surface layer.

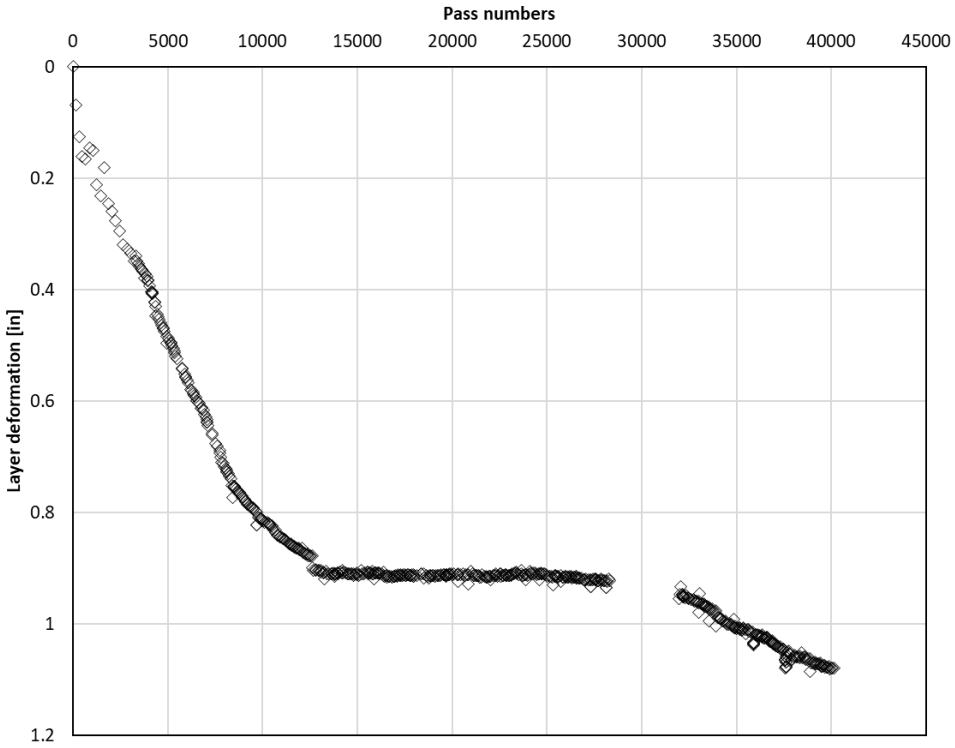

Figure 33. Accumulated Layer Deformation at LFS-1S P-209 Base Layer

Figure 34 presents the distance between the coil pairs throughout the 40,000 vehicle passes at the LFS-1N section. While the deflection trends are similar, the location of the maximum deflection was slightly different compared to the LFS-1S section. The maximum deflection of 0.173 in. (5.49% strain) was produced between CS 9 and CS 10 for LFS-1N, which is between 22-in. and 25-in. depth from the pavement's surface. The LFS-1S section showed a greater depth of maximum deformation compared to the LFS-1N section, likely due to the relatively lower thickness of HMA surface layer. Figure 35 shows the accumulation trends of permanent deformation for each 3-in. interval for the LFS-1N test section.

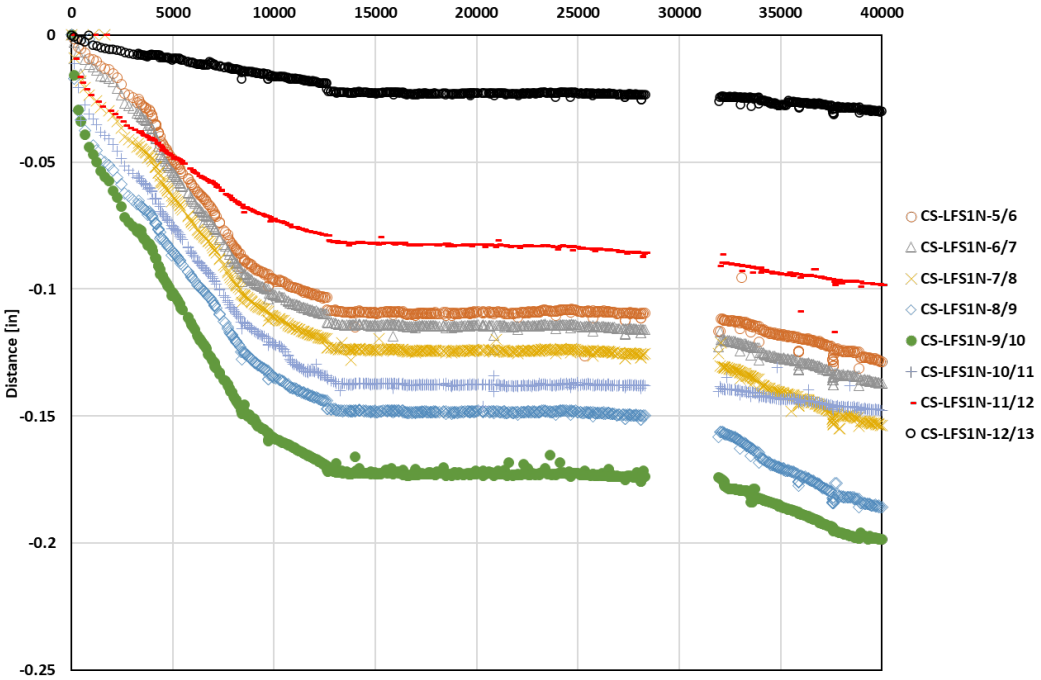

Figure 34. Change in Distance Between Coil Pairs vs Number of Passes at the P-209 Base Layer of LFS-1N

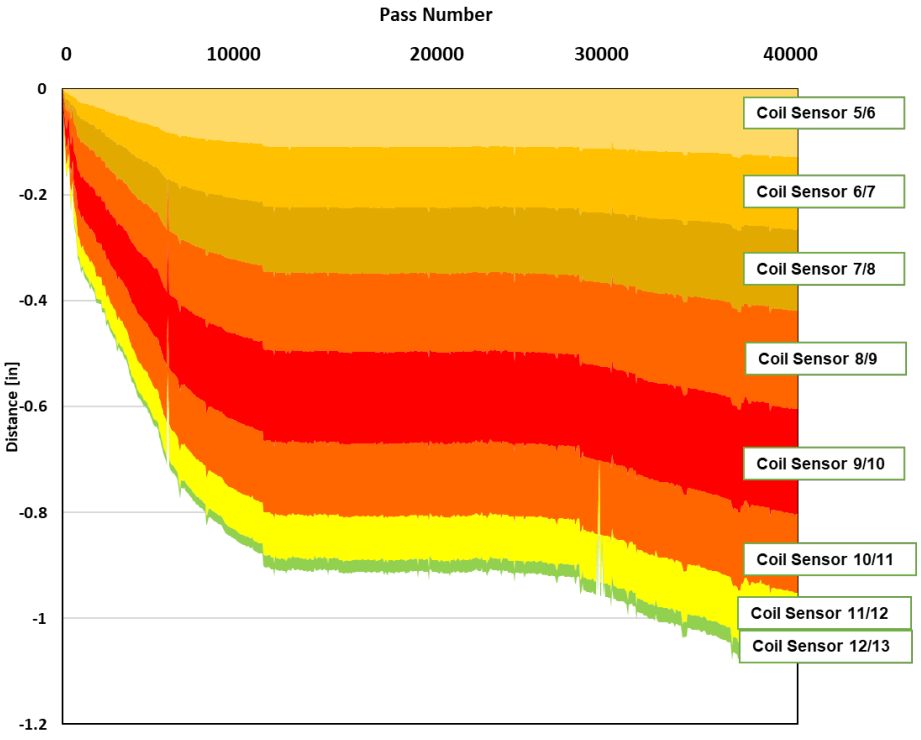

Figure 35. Accumulation Trends of Permanent Deformation for Each 3-in. Interval at the P-209 Base Layer of LFS-1N

3.3 VERTICAL STRAIN INFLUENCE FACTOR MODEL FOR P-209 BASE LAYER

Figure 36 shows the P-209 base layer deformations with a 3-in. interval after 26,400 passes. Clearly, both LFS-1N and LFS-1S test sections indicated that the maximum permanent deformation was generated toward the bottom of the base layer, which is not commonly considered a location for critical pavement response collection in mechanistic analyses of flexible pavements. This finding is in good agreement with the concept of vertical strain influence factor for the calculation of elastic settlement of shallow foundations over sand, introduced by Schmertmann (1970). Numerous researchers verified experimentally and empirically that the vertical strain profiles below rigid or flexible footings show the strain levels to peak at some depth below the footing base and then approach zero at greater depths (Janabi et al., 2022; Lee et al., 2008; O'Loughlin & Lehane, 2010; Schmertmann et al., 1978). Vertical permanent deformation data at 3-in. increments measured with CSs indicated that a similar strain profile was created in the P-209 layer under heavy dynamic aircraft gear loadings.

Figure 37 shows the application of the strain influence factor diagram by Schmertmann (1970) to the permanent deformation profile at LFS-1N, where I_z is the strain influence factor, I_{z0} is the I_z at the foundation level, I_{zp} is the peak I_z, z_p is normalized depth at peak I_z, z_l is the depth of the strain influence zone, and B is the width of the shallow foundation. The diagram clearly shows the existence of peak strain influence factor (I_{zp}) at a certain depth (z_p). The depth of the maximum deformation (z_p) was 3 in. higher for LFS-1N; likely due to the thicker HMA surface layer. Assuming B is the test vehicle wander width, the estimated z_p of CC9 test section is approximately 0.3. The z_p value from the previous studies on various types of foundations typically ranged between 0.3 and 1.7, with an average value of 0.47 (Pantelidis, 2020).

It is notable that the permanent deformation trend of the base layer measured by CSs was like that of the surface layer and showed small variations. Previous full-scale pavement response tests conducted at NAPTF used MDDs for measuring individual layer deformations reported the MDD readings not considering data separation by wander position, travel direction, and wander sequence, etc. seemed erratic and random (Donovan, 2009). MDDs collect displacement data during dynamic wheel loading by measuring the relative movement of the snap rings to the anchor, and thus the permanent deformation measurements are only available through dynamic response analysis after each pass. Therefore, the accumulated deformation was estimated by accumulating residual deformation at each pass (Sarker et al., 2019). On the other hand, coil sensors could measure the absolute distance between each sensor, which results in more stable data. Hence, CS data collection and utilization provide an effective vertical strain measurement tool for pavement response analysis, as well as an accurate means to determine permanent deformation damage accumulation mechanisms in thick granular layers.

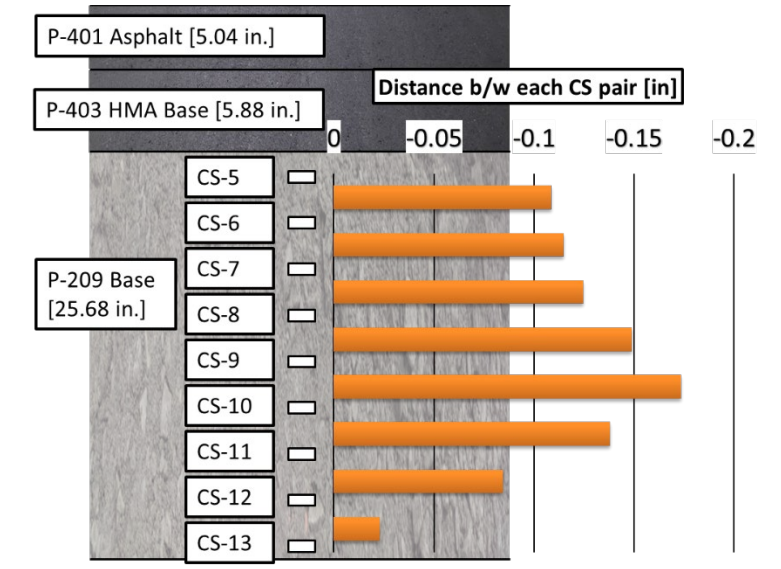

(a)

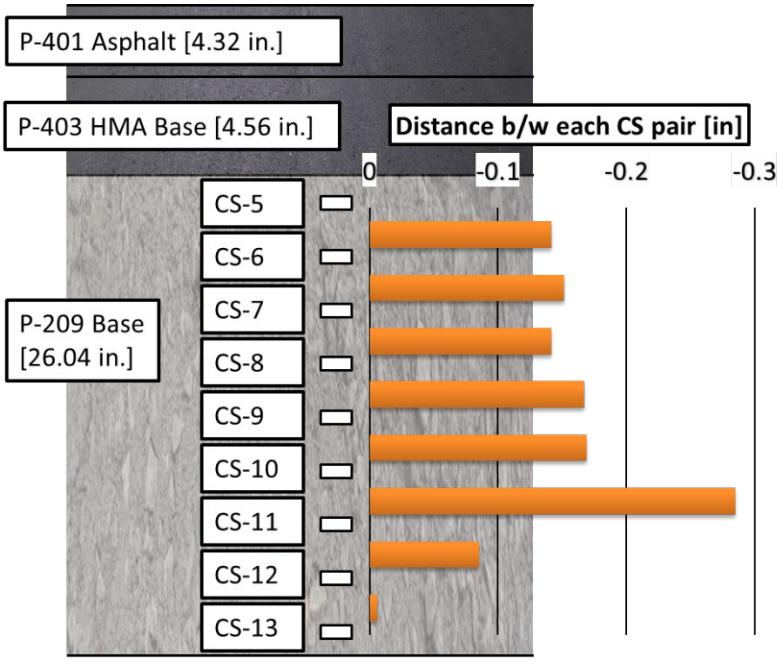

(b)

Figure 36. P-209 Base Layer Deformations with a 3-in. Interval for (a) LFS-1N and (b) LFS-1S after 26,400 Passes

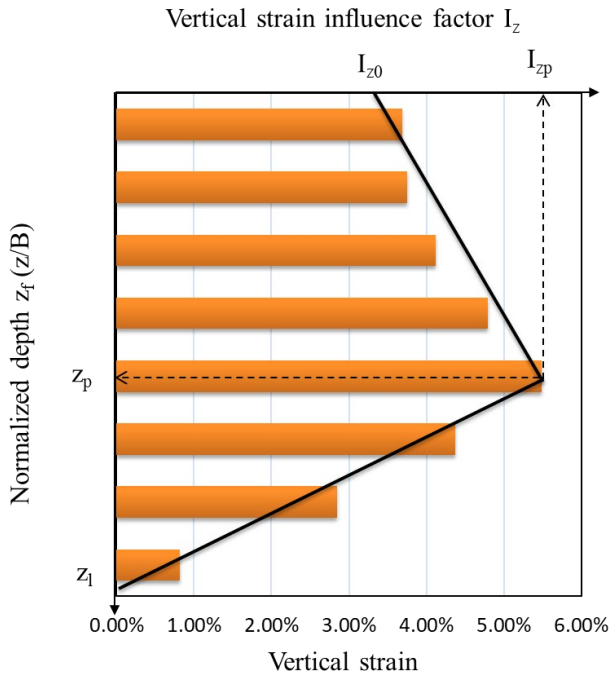

Figure 37. Base-Layer Deflection for LFS-1N with Strain Influence Factor Diagram (adapted from Schmertmann et al., 1978)

3.4 LFC-3S GEOSYNTHETICS AND LFC-4S CEMENT-TREATED DRAINABLE BASE

Figure 38 shows the cross-sections of LFC-3S and LFC-4S with CS arrays installed in the P-209 base layer. These two test items had CS arrays installed in the unbound base layer only at the south sections. Three pairs of inductive CSs were placed 3 in. apart throughout the aggregate base layer, and all sensors were installed under the centerline of the NAPTV gear path.

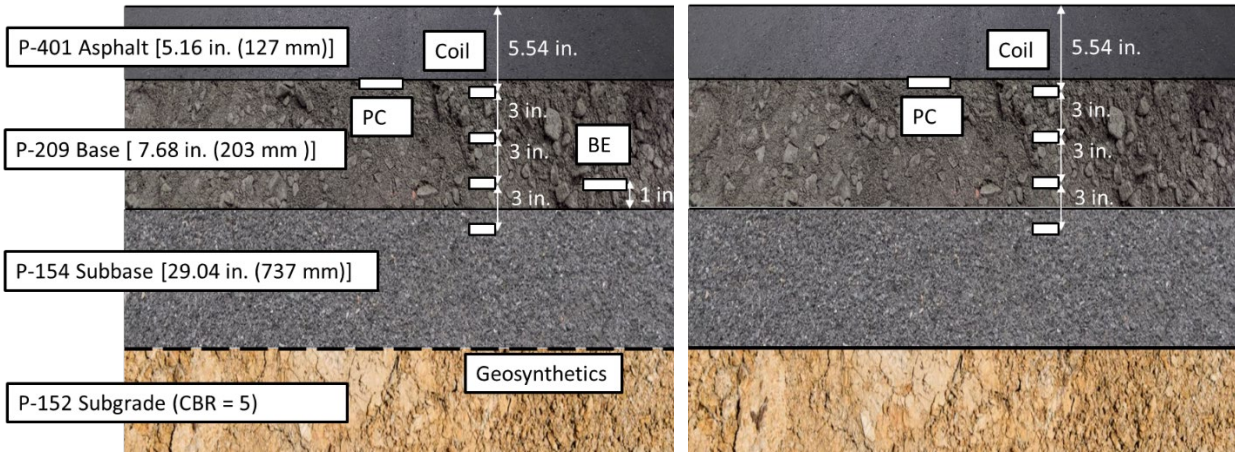

(a) (b)

Figure 38. Cross-Section View of (a) LFC-3S and (b) LFC-4S

Figures 39 and 40 show the distance between each CS pair measured throughout the 40,000 vehicle passes. In general, the deformation shows a similar trend to the LFS-1 section, i.e., deformation increased until approximately pass number 13,000, then the deflection rate decreased significantly after primary stabilization, then increased again after approximately 30,000 passes. The CS pair at the shallow depth, i.e., CS 5 and 6 pair at the LFS-3S and LFS-4S sections, were not functioning after 2,244 and 9,174 passes were applied, respectively. Considering the relatively thin thickness of the HMA surface layer in these sections (i.e., 5 in.), this is likely due to the influence of rutting in the upper HMA layer. The top CS was located near the bottom of HMA layer, and the CS pair at LFC-3S section, which showed excessive surface rutting compared to the LFC-4S section, stopped functioning earlier. Although the calculation of total deformation of the base layer is not feasible for these sections due to the CS sensor failure, the data collected from the CSs that survived traffic loading indicated a reasonable trend. The CS pair at the deeper depth, i.e., CS 7 and 8 pair at the LFC-4S section, indicated significantly lower deformation compared to the CS pair at the shallower depth.

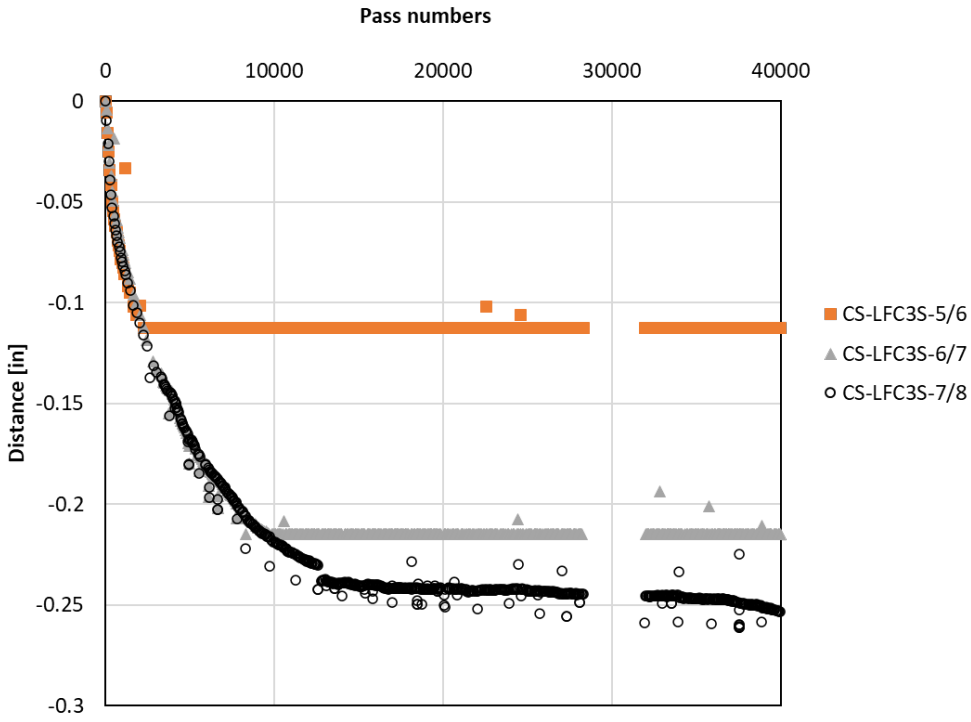

Figure 39. Distance Between Each Coil Sensor Pair at the LFC-3S Section

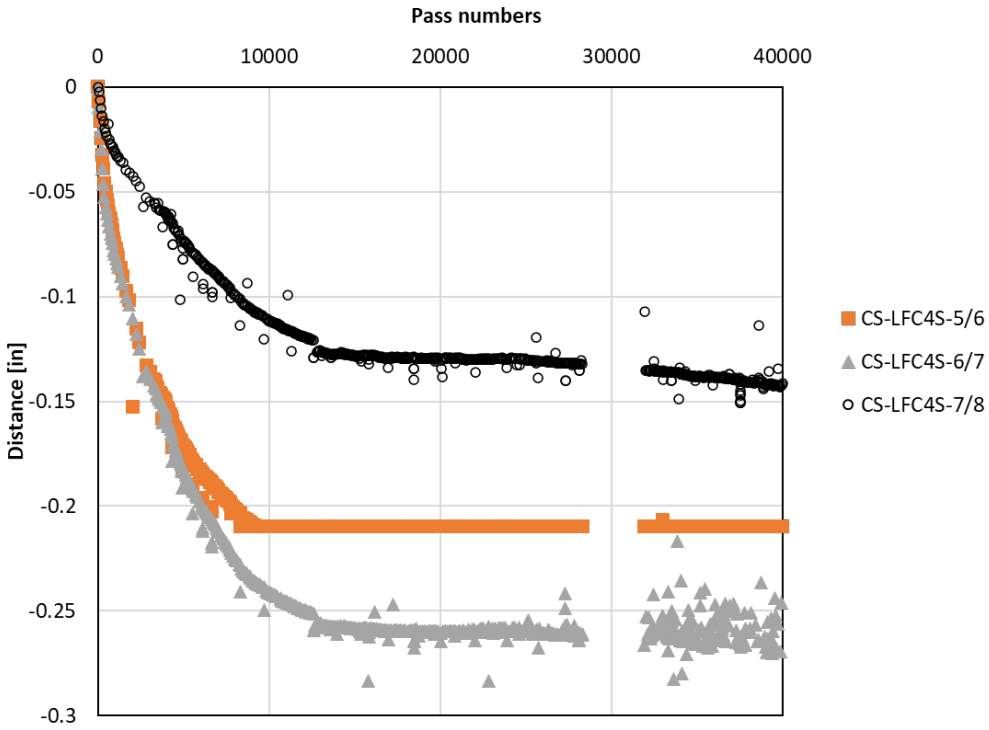

Figure 40. Distance Between Each Coil Sensor Pair at LFC-4S Section

3.5 SUMMARY

In the CC9 experiments, arrays of inductive CSs were embedded within the base layer along its depth as non-contact strain measurement devices for the P-209 base layer. Permanent deformation data were collected from these CSs, and the pavement surface rut data were recorded between each complete wander pattern during the initial 40,000 vehicle passes.

The data obtained from the coil sensors revealed an initial, constant increase in base layer deformation, followed by a steady-state zone as the pavement base layer consolidates and stabilizes over time and under traffic loading. The deflection rate increased again after approximately 30,000 passes. After 26,400 vehicle passes, the P-209 base layer of LFS-1N section deformed by 0.92 in. (representing 75.6% of the total permanent deformation), while the LFS-1S section experienced a deformation of 1.15 in. (composing 84.5% of the total deformation).

These CC9 experiment results align with previous NAPTF findings, emphasizing that most of the permanent deformation occurs in the relatively thick unbound aggregate base course layer(s). In particular, the maximum permanent deformation of 0.173 in. (equivalent to a 5.49 % strain) was observed between depths of 22 in. to 25 in. from the pavement surface at LFS-1N section. Meanwhile, the LFS-1S section exhibited a maximum deformation of 0.285 in. (corresponding to an 8.39 % strain) in the depth range between 25 to 28 in. from the pavement surface. In both sections, the maximum permanent deformation was concentrated toward the bottom of the base layer—specifically a 5.49% strain at a depth of 23.5 in. for section LFS-1N and an 8.39% strain at a depth of 26.5 in. for section LFS-1S. Consequently, the permanent deformation data, collected at 3-in. intervals via a CS array, demonstrated the applicability of the vertical strain influence factor for calculating the elastic settlement of shallow foundations in unbound aggregate layers subjected to heavy dynamic aircraft gear loadings. Notably, LFS-1N exhibited a lower magnitude of permanent deformation and a shallower depth for the maximum deformation, likely attributed to its thicker HMA layer. Furthermore, measurements from the CS in the base layer of LFC-3S and LFC-4S display a deformation trend similar to that of the LFS-1 section.

In conclusion, the findings from the NAPTF CC9 experiment affirm that coil sensors serve as effective tools for measuring vertical strains for pavement response analysis. These sensors accurately determine the accumulation of permanent deformation damage and associated mechanisms within thick granular layers. This technology enables the collection of stable measurements of base layer deformations at small intervals.

4. MODULUS QUANTIFIED USING COIL SENSOR AND PRESSURE CELL DATA FOR P-209 BASE AND P-154 SUBBASE LAYERS

4.1 MODULUS CALCULATION USING COIL SENSOR AND PRESSURE CELL

In previous sections, the modulus and deformation behavior of P-209 granular base layers in airport pavements measured using BE field sensors and CSs are discussed. In addition to the two types of sensors mentioned above, pressure cells (PCs) were also installed on top of the base and subbase layers of CC9 test sections. In this section, a novel approach to estimating the modulus

behavior of granular base using coil sensors and pressure cell data is discussed, referred to herein as the CS-PC method.

PCs measure the dynamic pressure changes in the surrounding material through the internal pressure change in a thin, hydraulic-fluid cell between the two flat metal plates. A transducer in the pressure cell converts the fluid pressure change into an electrical signal. The output voltage collected by the data acquisition system is converted to a pressure measurement according to an established correlation from the calibration. To minimize local plate deflection due to pressure exerted from surrounding particles, the PCs used in this research are equipped with additional thick plates on each side [see Figure 41(b)].

(a) (b)

Figure 41. Embedded Sensors at NAPTF CC9: (a) Inductive CS Pairs and (b) PC

4.2 LFC-3 P-209 BASE LAYER

Figure 38(a) shows the CS array and the PC installed in the LFC-3S P-209 base layer. The PC installed on top of the base is designed to measure dynamic pressure changes in the surrounding material. Figure 42 shows a typical dynamic response from a CS and a PC installed in the base layer of LFC-3S during Pass No. 11 of the traffic test. The three peaks observed from both sensors correspond to loads from the three wheels of the tridem-axle gear of the NAPTV passing over the sensors. The resilient modulus (M_R) of the unbound aggregate material is calculated as applied vertical deviator stress divided by recoverable strain as shown in Equation 4. Hence, the M_R of the base layer can be calculated using the wheel load deviator stress obtained from the pressure cell and the recoverable resilient strain collected from coil sensors.

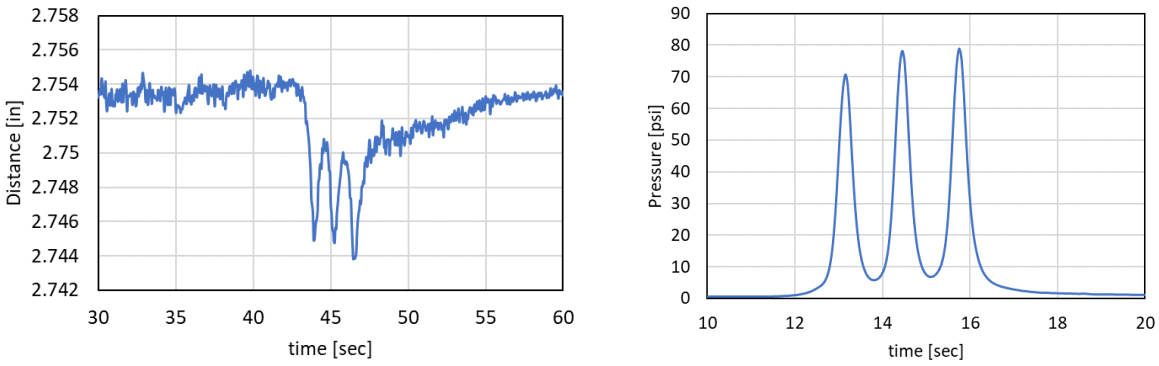

(a) (b)

Figure 42. Typical Dynamic Responses from Embedded Sensors showing the (a) CS and (b) PC Measurements during Pass 11 (Wander 1)

As shown in Figure 22, as the wheel track changes in each wander, the stress states induced in the aggregate base layer will vary. In this experiment, responses under wheel track -2, 2, 3, and -3, which all have one of the wheels coinciding with the sensor location, were selected to calculate the resilient moduli. These wheel tracks induce the primary stress path in the vertical orientation with the load applied being directly on top and, therefore, yield a fair comparison considering that resilient modulus is a stress-path dependent property of aggregates (Tutumluer & Seyhan, 1999; Tutumluer & Thompson, 1997). Note that pressure data after pass number 330 were not used due to issues with data recordings.

Figure 43 presents the resilient moduli calculated using the CS and PC data in addition to the BE field sensor results until Wander No. 5. The moduli measured using two different approaches were comparable and fell into the typical modulus range for crushed aggregates used in base layers (AASHTO, 2020; Puppala, 2008; Tutumluer, 2013). This result confirms that both BE field sensor and CS-PC methods can estimate the in situ resilient moduli reasonably well. Note that the CS-PC method requires dynamic pulsing to calculate the modulus, thus the modulus before traffic loading (i.e., Pass 0) cannot be calculated using the CS-PC method.

It is notable that the resilient moduli from the CS-PC method show a zigzag pattern ranging from 20 to 40 ksi (137.90 to 275.79 MPa). As summarized in Table 6, a two-way pass of the test vehicle was made at each wheel track. In Figure 22, the filled-circle symbols represent the first pass (eastbound) and the empty-circle symbols represent the second-pass (westbound) loading applied at the same location. In all passes, the first (eastbound) pass always showed a lower modulus compared to the modulus from the second (westbound) pass. On average, the modulus from the second pass was 28.24% higher than that of the first pass. The previous NAPTF full-scale pavement tests reported that the vehicle passes with wander offsets caused an “anti-shakedown” effect in the unbound aggregate layer due to the upward dilative deformation caused by large horizontal stresses (Donovan et al., 2016; Donovan, 2009; Donovan & Tutumluer, 2008; Sarker & Tutumluer, 2018). Further, Kang et al. (2022b & 2023) observed a modulus decrease after the wheel pass with the wheel offset and a modulus increase after the wheel pass without the wheel offset via BE field sensor measurement.

Figure 16 summarizes the effect of wheel pass with and without offsets. As wheel tracks -2, 2, 3, and -3 were always preceded by passes with offset, the upward dilative deformation (anti-shakedown) results in the low stiffness from the first pass of the CS-PC measurement. The higher modulus from the second pass, therefore, benefits from the compression of aggregates (shakedown) during the first pass. This zigzag trend of the modulus from the CS-PC method is in accordance with the previous findings using BE field sensor and layer deflection methods, confirming the vehicle wander effects on the aggregate behavior.

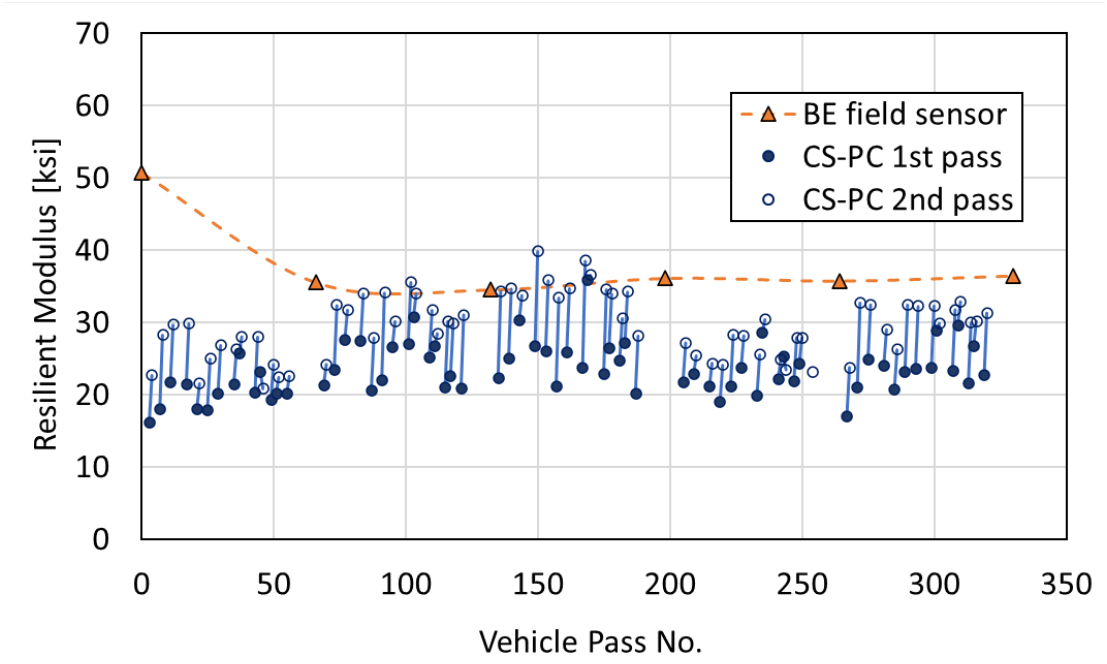

Figure 43. Resilient Moduli Estimated from Embedded Field Sensors during the CC9 Traffic Test for LFC-3 P-209 Base Layer

4.3 LFC-3 P-154 SUBBASE LAYER

Figure 44 shows the cross-sections of LFC-3 showing embedded sensors in subbase layer. The embedded sensors were installed towards the upper part of the subbase layer near the geogrid location.

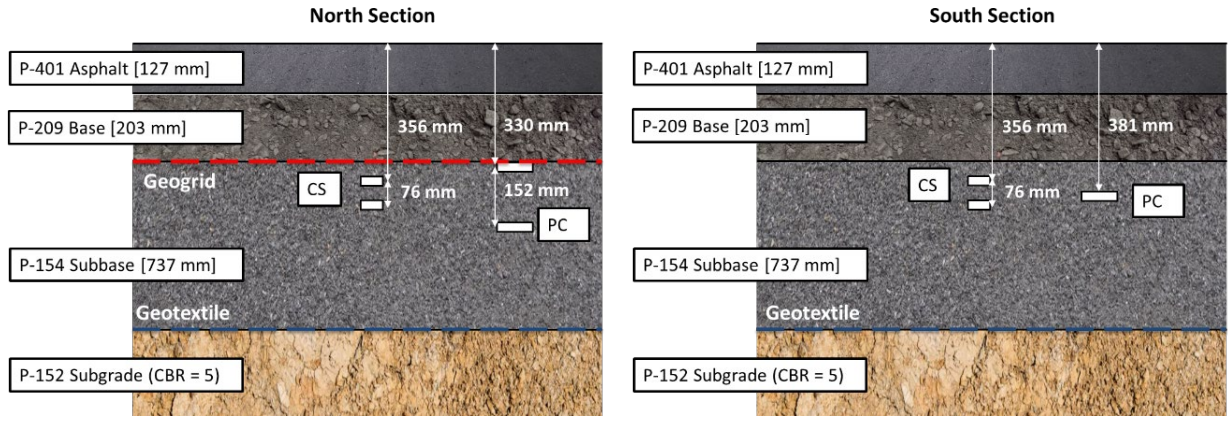

(a) (b)

Figure 44. Cross-Sections of LFC-3 Showing Embedded Sensors in Subbase Layer for (a) the LFC-3N Geogrid Stabilized and (b) the LFC-3S Unstabilized Control Sections

Figure 45 shows the properties of the P-154 subbase course, carbonate-based, manufactured aggregate screenings. Sieve analysis was conducted in accordance with the ASTM C136 (2020) procedure to determine the grain-size distribution curve shown in Figure 45(a). The subbase material is classified as A-1-b (stone fragments, gravel, and sand) according to the AASHTO soil classification system, and as SP-SM (poorly graded sand with silt and gravel) according to the Unified Soil Classification System (USCS). The mean grain size (D_{50}) of the aggregate material is 1.42 mm (0.056 in.) and the particle fraction passing No. 200 (0.075 mm) sieve size is 10.2%. As shown in Figure 7(b), the maximum dry density and optimum moisture content (OMC) determined by the modified Proctor compaction test (ASTM D1557-07, 2010) were 21.96 kN/m^3 (141 pcf) and 7.9%, respectively.

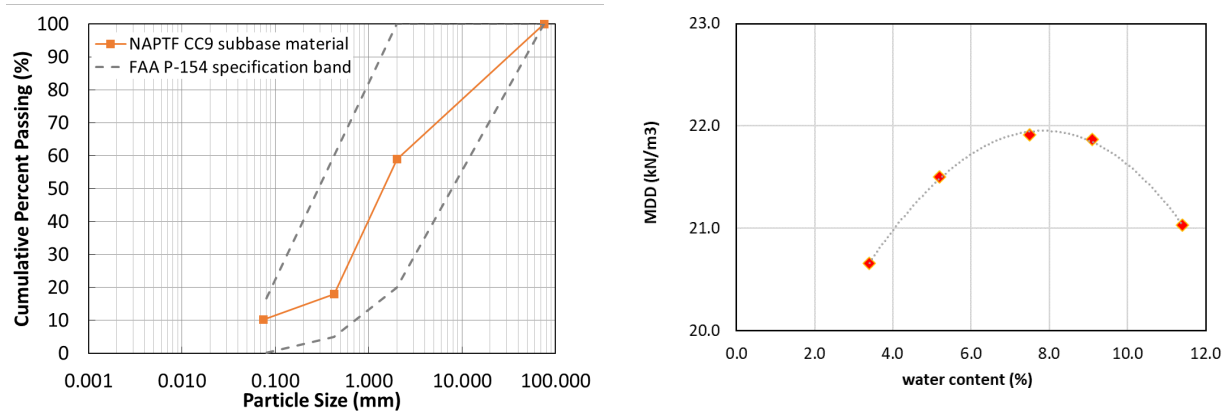

(a) (b)

Figure 45. Properties for the P-154 Subbase Coarse Aggregate: (a) Grain-Size Distribution and (b) Moisture-Density Relationship

A pair of inductive coil sensors were installed at the top of the subbase layer of both LFC-3N and LFC-3S test sections, as shown in Figure 44. PCs were installed in the subbase layer, two in LFC-3N and one in LFC-3S sections. Throughout 330 vehicle passes, dynamic pavement

responses, i.e., applied pressure levels, were monitored using PCs. The LFC-3N pressure values were calculated by averaging the pressure from the two installed PCs to obtain an accurate estimate of the pressure at the same depth as the coil sensor.

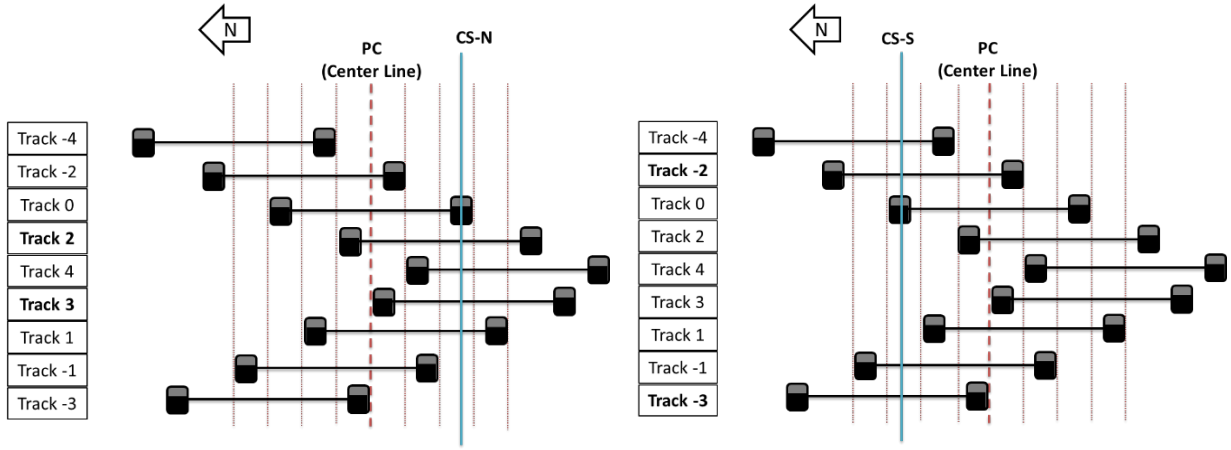

Figure 46. Traffic Loading Procedure with Wander Patterns for (a) LFC-3N and (b) LFC-3S Test Sections

The stress states induced in the subbase layer vary as the NAPTV loading is applied at different wander positions. Track 2 of LFC-3N and Track -2 of LFC-3S induce the same stress state at the sensor locations (see Table 6 and Figure 46). Figure 47 shows the resilient moduli estimated from vehicle passes at Track 2 of LFC-3N and at Track -2 of LFC-3S. Clearly, the estimated moduli at the geogrid-stabilized section indicated higher values with an average resilient modulus improvement of 68.7%. Therefore, it could be concluded that the geogrid-stabilized subbase layer has higher stiffness near the geogrid location. The authors previously reported that the extent of the geogrid-stiffened zone in the CC9 test section base layer was approximately 102 mm (4 in.) from the geogrid location (Kang et al., 2022a). The sensors located within the geogrid-stiffened zone captured the stiffness improvement achieved through geogrid-aggregate interlocking. Note that the coil sensors were located 0.69 m (2.25 ft) apart from the PC (see Figure 44). Although the vertical pressure values were collected near the wheel path, the CS deflections were measured 0.52 m (1.71 ft) apart from the wheel path, and, thus, the estimated moduli values could be higher than the actual values.

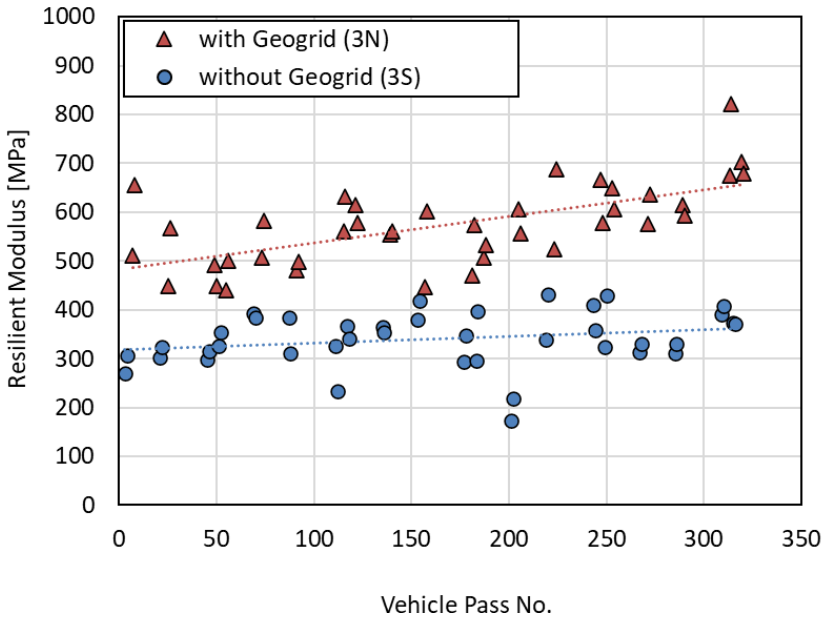

Figure 47. Resilient Moduli Estimated using CS-PC Method: Moduli from Track 2 of LFC-3N and Track -2 of LFC-3S

Figure 48 presents the resilient moduli estimated from vehicle passes at Track 3 of LFC-3N and at Track -3 of LFC-3S, which had the same stress state. Similarly, the estimated moduli at the geogrid-stabilized section were higher, with an average improvement of 155.3%. The estimated moduli from Tracks 3 and -3 were higher than those from Tracks 2 and -2 due to the larger horizontal distance of the CS from the wheel path, which was 0.59 m (1.94 ft), meaning the measured vertical strain was an underestimate of the actual strain at the pressure cell location. Notably, the estimated moduli increased as the number of load repetitions increased, especially at the geogrid-stabilized section. This could be attributed to the stabilized unbound aggregate layer by rearranging the aggregate particles during load repetitions, especially during the first few load repetitions (Kang et al., 2022b). Han et al. (2020) reported that from a falling weight deflectometer (FWD) test performed before and after accelerated pavement testing (APT), the modulus of the unbound base course for a geogrid-stabilized pavement after APT was considerably higher than the unstabilized section due to the fully mobilized benefit of geogrid. A higher modulus increase observed in the geogrid-stabilized section was likely due to the gradual mobilization of the geogrid during vehicle passes.

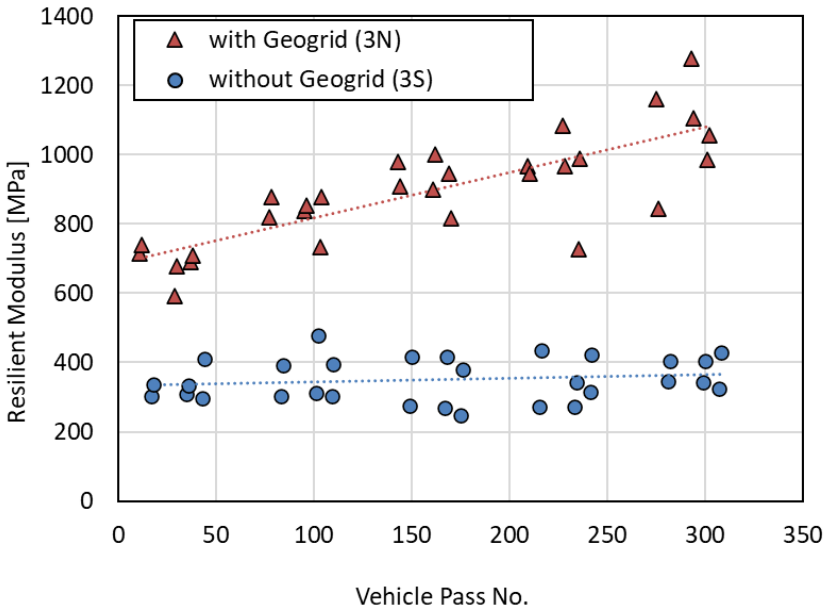

Figure 48. Resilient Moduli Estimated using CS-PC Method: Moduli from Track 3 of LFC-3N and Track -3 of LFC-3S

4.4 SUMMARY

This experiment introduced a novel method for characterizing the stiffness of airport pavement base layers by using embedded inductive CSs and PCs. These sensors record dynamic responses during vehicle traffic passes on the pavement test section.

The in situ resilient modulus of the aggregate base layer was assessed during the NAPTF traffic test. Two methods were employed for comparison:

(1) Deriving the modulus using shear wave velocities measured by BE field sensors and the established correlations.
(2) Directly calculating the modulus using in situ deformations and stress states determined from CS and PC data.

The moduli obtained from the CS and PC data, referred to as the CS-PC method, fell within the typical range for unbound aggregates commonly used in airport pavement base courses. Furthermore, similar moduli obtained from both the CS-PC and BE field sensor methods demonstrate their suitability for continuous monitoring and evaluation of in situ aggregate layer moduli.

The resilient moduli obtained using the CS-PC method exhibited a zigzag pattern, ranging from 20 to 40 ksi (137.90 to 275.79 MPa). Notably the moduli from the second shakedown pass were on average 28.24% higher than those from the first pass in the same wander position. This observation aligns with the previously reported “anti-shakedown” effect resulting from wheel wander, especially in the initial pass with offset wheel loads.

Furthermore, estimated subbase moduli from the geogrid-stabilized section were on average 68.7% to 155.3% higher than those from the unstabilized section. This indicates a significant stiffness improvement within the 102-mm (4-in.) geogrid-stiffened zone. Resilient moduli increase with the number of passes, particularly for the geogrid-stabilized section, attributed to the gradual strengthening effect of stabilization during vehicle passes.

These research findings underscore the benefits of geogrid stabilization in airport pavements, enhancing lateral restraint and stiffness in unbound aggregate base/subbase layers.

5. SUMMARY AND CONCLUSIONS

This research focused on collecting data from embedded sensors—specifically, bender element (BE) field sensors, inductive coil sensors (CSs), and pressure cells (PCs)—during the FAA National Airport Pavement Test Facility (NAPTF) Construction Cycle 9 (CC9) experiments. The aim was to establish a data-driven approach for analyzing the modulus and deformation behavior of the P-209MR granular base and the P-154MR subbase layers in airport pavements.

Three BE field sensors were installed in the P-209 base layer of the geosynthetics test section (LFC-3), while the remaining sensors were placed in the fatigue model test section (LFS-1) and the cement-treated, drainable base test section (LFC-4). Prior to the traffic test stage, five stages of static and dynamic aircraft gear loadings were conducted as part of the pre-traffic tests for the CC9 test sections. Subsequently, during the traffic test, the National Airport Pavement Test Vehicle (NAPTV) applied dynamic gear loading of 58,000 lb (26.3 tons) per wheel to each test section. The traffic loading followed a wander pattern consisting of 66 vehicle passes in nine different positions. Dynamic responses from the sensors were collected using CSs and the PCs, while BE field sensor measurements were taken after the vehicle completed 66 passes within one wander pattern of traffic loading. The experiment evaluated the in situ resilient modulus of the aggregate base layer during the NAPTF traffic test.

Two methods were employed to study the resilient modulus of the aggregate base layer during the NAPTF traffic test. The first method estimated modulus from shear wave velocities (V_S) measured by BE field sensor and established correlations. The second method involved direct calculation using in situ deformations and stress states derived from CS and PC data, referred to as CS-PC method. These methods allowed for detailed analyses of the stiffness characteristics of the airport pavement base layer.

The results showed clear stress-hardening trends in the unbound aggregate base layer when estimated from shear wave velocities measured with varying levels of static loading. Depending on the vehicle's wander location, the behavior of aggregates, reflecting the "anti-shakedown" effect, exhibited either dilation or compression. The experiment also quantified stiffness changes resulting from dynamic wheel tests with specific load wander patterns through shear wave velocity measurements. Additionally, moduli from the CS-PC method displayed a zigzag pattern within a range of 20 to 40 ksi (137.90 to 275.79 MPa). The moduli from the second shakedown pass were approximately 28.24% higher, on average, than those from the first pass in the same wander position, confirming the previously reported "anti-shakedown" effect.

Moduli measurements from the embedded BE field sensors and the CS-PC method during the traffic tests exhibited good agreement and fell within the typical modulus range of unbound aggregates used in pavement base layers. However, the modulus of the base layer notably decreased after the initial wander sequence of the traffic tests due to particle rearrangement. At one test section (LFC-3S), a gradual recovery of the modulus was observed after loading up to 10,000-wheel passes, indicating stabilization. In contrast, another section (LFC-3N) showed minimal modulus recovery, likely due to excessive rutting observed during traffic tests.

The CS-PC method provided estimates of subbase moduli, revealing that geogrid-stabilized sections exhibited stiffness improvements ranging from 68.7% to 155.3% compared to unstabilized or conventional sections. Stiffness enhancement within the 102-mm (4-in.) geogrid-stiffened zone was evident from the BE field sensor measurements. Resilient moduli increased with the number of passes, especially in the geogrid-stabilized section, as the effects of stabilization gradually intensified.

Permanent deformation data from CSs were collected between each complete wander pattern over the first 40,000 vehicle passes. CS data indicated an initial constant increase in base layer deformation, followed by a steady-state zone as the pavement base layer stabilized. Deflection rates increased again after approximately 30,000 passes. Most permanent deformations in the CC9 experiment occurred in the thick, unbound, aggregate base course, consistent with previous NAPTF findings. The ability of CSs to measure deformation at small intervals suggested that the vertical strain influence factor for calculating elastic settlement of shallow foundations could be applied to unbound aggregate layers subjected to heavy dynamic aircraft gear loadings, with maximum vertical strains occurring toward the lower end of the base layer.

The NAPTF CC9 experiment yielded valuable insights into the influence of load wander patterns, the impact of dynamic loading on base moduli, deformation characteristics of the granular base with depth profiles, and the effect of geogrid stabilization on stiffness. Embedded sensor technology played a crucial role in these findings. Consequently, the embedded sensors proved highly effective in quantifying the behavior of granular base/subbase layers in airport pavements under diverse loading conditions. Future studies using embedded sensors will likely enhance our understanding of the modulus and deformation behavior of airport pavements, particularly when assessing the potential use of local aggregate materials and their mechanical stabilization alternatives using geosynthetics.

6. REFERENCES

American Association of State Highway and Transportation Officials (AASHTO). (2020). *Mechanistic-empirical pavement design guide: A manual of practice* (3rd ed.). https://store.transportation.org/Item/CollectionDetail?ID=196

AASHTO M145-91 (2012). Classification of Soils and Soil-Aggregate Mixtures for Highway Construction Purposes. Washington DC: American Association of State Highway and Transportation Officials.

AASHTO T307-99 (2003). Standard Method of Test for Determining the Resilient Modulus of Soils and Aggregate Materials. American Association of State Highway and Transportation Officials, Washington DC.

ASTM C136/C136M-19 (2020). Standard Test Method for Sieve Analysis of Fine and Coarse Aggregates. ASTM.org, DOI: 10.1520/C0136_C0136M-19

ASTM D2487-17 (2020). Standard Practice for Classification of Soils for Engineering Purposes (Unified Soil Classification System), DOI: 10.1520/D2487-17

ASTM D1557-07 (2010). Standard Test Methods for Laboratory Compaction Characteristics of Soil Using Modified Effort [56,000 ft-lbf/ft^3 (2,700 kN-m/m^3)], DOI: 10.1520/D1557-07

ASTM E1703/E1703M-10 (2015). Standard Test Method for Measuring Rut-Depth of Pavement Surfaces Using a Straightedge, DOI: 10.1520/E1703_E1703M-10R15

Byun, Y.-H., Feng, B., Qamhia, I. I. A. & Tutumluer, E. (2020). Aggregate properties affecting shear strength and permanent deformation characteristics of unbound–Base course materials. *Journal of Materials in Civil Engineering*, *32*(1), Article 04019332. https://doi.org/10.1061/(ASCE)MT.1943-5533.0003000

Clayton, C. R. I. (2011). Stiffness at small strain: research and practice. *Géotechnique*, *61*(1), 5–37. https://doi.org/10.1680/geot.2011.61.1.5

Donovan, P. R. (2009). *Analysis of unbound aggregate layer deformation behavior from full scale aircraft gear loading with wander* [Doctoral dissertation, University of Illinois at Urbana-Champaign]. Illinois Digital Environment for Access to Learning and Scholarship (IDEALS). https://hdl.handle.net/2142/83400

Donovan, P. R., & Tutumluer, E. (2008, August 25–27). The anti-shakedown effect. In E. Ellis, H.-S. Yu, G. McDowell, A.R Dawson, & N. Thom (Eds.), *Advances in Transportation Geotechnics— Proceedings of the 1st International Conference on Transportation Geotechnics*, Nottingham, UK, 111–116. CRC Press. https://doi.org/10.1201/9780203885949

Donovan, P., Sarker, P., & Tutumluer, E. (2016). Rutting prediction in airport pavement granular base/subbase: A stress history based approach. *Transportation Geotechnics*, *9*, 139–160. https://doi.org/10.1016/j.trgeo.2016.08.005

FAA Reauthorization Act of 2018, Pub. L. No. 115–254, 132 Stat. 3186 §525. (2018, October 5). https://www.congress.gov/bill/115th-congress/house-bill/302

FAA. (2021, June 7). *Airport pavement design and evaluation* (AC 150/5320-6G). U.S. Department of Transportation. https://www.faa.gov/documentLibrary/media/Advisory_Circular/150-5320-6G-Pavement-Design.pdf

Garg, N., & Hayhoe, G. F. (2003, January 14). *Permanent deformation behavior of the granular layers tested at the FAA's National Airport Pavement Test Facility*. 82nd Annual Meeting of the Transportation Research Board Modeling of Granular Bases for Flexible Pavements Session-556, Washington, DC. https://www.airporttech.tc.faa.gov/Products/Airport-Pavement-Papers-Publications/Airport-Pavement-Detail/permanent-deformation-behavior-of-the-granular-layers-tested-at-the-faas-national-airport-pavement-test-facility

Garg, N., Pecht, F., & Jia, Q. (2010). *Subgrade stress measurements under heavy aircraft gear loading at FAA National Airport Pavement Test Facility.* Paving Materials and Pavement Analysis, Proceedings of the GeoShanghai 2010, 484–491. Shanghai, China. https://doi.org/10.1061/41104(377)62

Garg, N., & Thompson, M. R. (1997). Triaxial characterization of Minnesota road research project granular materials. *Transportation Research Record*, *1577*(1), 27–36. https://doi.org/10.3141/1577-04

Greenslade, F., Alabaster, D., Steven, B., & Pidwerbesky, B. (2012). The CAPTIF unbound pavement strain measurement system. In D. Jones, J. Harvey, I.L. Al-Quadi, & A. Mateos (Eds.) *Advances in Pavement Design through Full-scale Accelerated Pavement Testing* (1st ed. pp. 113–120). CRC Press.

Han, B., Polaczyk, P., Gong, H., Ma, R., Ma, Y., Wei, F., & Huang, B. (2020). Accelerated pavement testing to evaluate the reinforcement effect of geogrids in flexible pavements. *Transportation Research Record*, *2674*(10), 134–145. SAGE Publications Inc. https://doi.org/10.1177/0361198120935120

Hayhoe, G. F. (2004, September 26–29). Traffic testing results from the FAA's National Airport Pavement Test Facility. *Proceedings of the 2nd International Conference on Accelerated Pavement Testing*. University of Minnesota, Minneapolis, MN, United States.

Hayhoe, G. F., Garg, N., & Dong, M. (2012). "Permanent deformations during traffic tests on flexible pavements at the National Airport Pavement Test Facility. *Airfield Pavements: Challenges and New Technologies*, 147–169. https://doi.org/10.1061/40711(141)10

Hicks, R. G., & Monismith, C. L. (1971). Factors influencing the resilient response of granular materials. *Highway Research Record*, Issue 345, 15–31. https://onlinepubs.trb.org/Onlinepubs/hrr/1971/345/345-002.pdf

Ishibashi, I., & Zhang, X. (1993). unified dynamic shear moduli and damping ratios of sand and clay. *Soils and Foundations*, *33*(1), 182–191. https://doi.org/10.3208/sandf1972.33.182

Janabi, F. H., Sakleshpur, V. A., Prezzi, M., & Salgado, R. (2022). Strain influence diagrams for settlement estimation of square footings on layered sand. *Journal of Geotechnical and Geoenvironmental Engineering*, *148*(5), Article 04022025. https://doi.org/10.1061/(ASCE)GT.1943-5606.0002770

Kang, M., Kim, J. H., Qamhia, I. I. A., Tutumluer, E., & Wayne, M. H. (2020). Geogrid stabilization of unbound aggregates evaluated through bender element shear wave measurement in repeated load triaxial testing. *Transportation Research Record*, *2674*(3), 113–125. https://doi.org/10.1177/0361198120908230

Kang, M., Qamhia, I. I. A., Tutumluer, E., Flynn, M., Garg, N., & Villafane, W. (2022a). "Near geogrid stiffness quantification in airport pavement base layers using bender element field sensor. In E. Tutumluer, S. Nazarian, I. Al-Qadi, and I. I. A. Qamhia (Eds.), *Advances in Transportation Geotechnics IV*, *Lecture Notes in Civil Engineering* (Vol. 165), 703–715. https://doi.org/10.1007/978-3-030-77234-5_58

Kang, M., Qamhia, I. I. A., Tutumluer, E., Garg, N., & Villafane, W. (2022b). Airport pavement stiffness monitoring and assessment of mechanical stabilization using bender element field sensor. *Transportation Research Record*, *2676*(8), 542–553. https://doi.org/10.1177/03611981221084685

Kang, M., Qamhia, I. I. A., Tutumluer, E., Hong, W.-T., and Tingle, J. S. (2021). Bender element field sensor for the measurement of pavement base and subbase stiffness characteristics. *Transportation Research Record*, *2675*(8), 394–407. https://doi.org/10.1177/0361198121998350

Kang, M., Wang H., Qamhia, I. I. A., & Tutumluer, E. (2022). Modulus properties of granular materials at various strain levels from repeated load triaxial testing with bender elements. *Geo-Congress 2022*, 420–430. https://doi.org/10.1061/9780784484067.042

Kang, M., Wang, H., Qamhia, I. I. A., Tutumluer, E., Garg, N., Villafane, W., & Murrell, S. (2023). Evaluation of airport pavement base layer stiffness characteristics via embedded field sensors. *Transportation Research Record*, *2677*(8), 462–473. https://doi.org/10.1177/03611981231156938

Kwon, J., & Tutumluer, E. (2009). Geogrid base reinforcement with aggregate interlock and modeling of associated stiffness enhancement in mechanistic pavement analysis. *Transportation Research Record*, *2116*(1), 85–95. https://doi.org/10.3141/2116-12

Lee, J., Eun, J., Prezzi, M., & Salgado, R. (2008). Strain influence diagrams for settlement estimation of both isolated and multiple footings in sand. *Journal of Geotechnical and Geoenvironmental Engineering*, *134*(4), 417–427. https://doi.org/10.1061/(ASCE)1090-0241(2008)134:4(417)

Lee, J.-S., & Santamarina, J. C. (2005). Bender elements: Performance and signal interpretation. *Journal of Geotechnical and Geoenvironmental Engineering*, *131*(9), 1063–1070. https://doi.org/10.1061/(ASCE)1090-0241(2005)131:9(1063)

Mishra, D., & Tutumluer, E. (2012). Aggregate physical properties affecting modulus and deformation characteristics of unsurfaced pavements. *Journal of Materials in Civil Engineering*, *24*(9), 1144–1152. https://doi.org/10.1061/(ASCE)MT.1943-5533.0000498

O'Loughlin, C. D., & Lehane, B. M. (2010). Nonlinear Cone Penetration Test-Based Method for Predicting Footing Settlements on Sand. *Journal of Geotechnical and Geoenvironmental Engineering*, *136*(3), 409–416. https://doi.org/10.1061/(ASCE)GT.1943-5606.0000228

Pantelidis, L. (2020). A critical review of Schmertmann's strain influence factor method for immediate settlement analysis. *Geotechnical and Geological Engineering*, *38*, 1–18. https://doi.org/10.1007/s10706-019-01062-1

Puppala, A. J. (2008). Estimating stiffness of subgrade and unbound materials for pavement design. *National Cooperative Highway Research Program* (*NCHRP) Synthesis 382—A Synthesis of Highway Practice*. Transportation Research Board/National Academies Press. https://doi.org/10.17226/13598

Qamhia, I. I. A., Chow, L. C., Mishra, D., & Tutumluer, E. (2017). Dense-graded aggregate base gradation influencing rutting model predictions. *Transportation Geotechnics* [SI: Pavement Geotechnics], *13*, 43–51. https://doi.org/10.1016/j.trgeo.2017.07.002

Rada, G., & Witczak, M. W. (1981). Comprehensive evaluation of laboratory resilient moduli results for granular material. *Transportation Research Record*, Issue 810, 23–33. https://onlinepubs.trb.org/Onlinepubs/trr/1981/810/810-004.pdf

Santamarina, J. C., Klein, K.A., and Fam, M.A. (2001). *Soils and waves: Particulate materials behavior, characterization, and process monitoring*. J. Wiley & Sons.

Sarker, P. (2020). Analyses and prediction of granular layer rutting trends in airport pavements due to heavy aircraft wheel loading and wander patterns [Doctoral dissertation, University of Illinois at Urbana-Champaign]. Illinois Digital Environment for Access to Learning and Scholarship (IDEALS). https://www.ideals.illinois.edu/items/115557

Sarker, P., & Tutumluer, E. (2018). Airfield pavement damage evaluation due to new-generation aircraft wheel loading and wander patterns. *Transportation Research Record*, *2672*(29), 82–92. https://doi.org/10.1177/0361198118799705

Sarker, P., & Tutumluer, E. (2020). *A stress-history-based approach for predicting deformation potentials of granular base and subbase layers in airport pavements*. Illinois Center for Transportation Report, ICT-20-013, June, 197. https://apps.ict.illinois.edu/projects/getfile.asp?id=9253

Sarker, P., Tutumluer, E., & Garg, N. (2019, July 21–24). Analyses of airport pavement rutting trends in FAA's NAPTF Construction Cycle 5 pavement test sections. In I. Al-Qadi, H. Ozer, A. Loizos, &S. Murrell (Eds*.) Airfield and Highway Pavements 2019: Innovation and Sustainability in Highway and Airfield Pavement Technology* [Symposium], 407–417. International Airfield and Highway Pavements Conference 2019, Chicago, IL, United States. https://doi.org/10.1061/9780784482476.040

Schmertmann, J. H. (1970). Static cone to compute static settlement over sand. *Journal of the Soil Mechanics and Foundations Division*, *96*(3), 1011–1043 https://doi.org/10.1061/JSFEAQ.0001418

Schmertmann, J. H., Hartman, J. P., & Brown, P. R. (1978). Improved strain influence factor diagrams. *Journal of the Geotechnical Engineering Division*, *104*(8), 1131–1135. https://doi.org/10.1061/AJGEB6.0000683

Seed, H. B., & Idriss, I. M. (1970). *Soil Moduli and Damping Factors for Dynamic Response Analyses* (Report No. EERC 70-10). Earthquake Engineering Research Center. https://ntrl.ntis.gov/NTRL/dashboard/searchResults/titleDetail/PB197869.xhtml

Thompson, M. R., & Smith, K. L. (1990). Repeated triaxial characterization of granular bases. *Transportation Research Record*, Issue 1278, 7–17. https://onlinepubs.trb.org/Onlinepubs/trr/1990/1278/1278-002.pdf

Tutumluer, E. (2013). Practices for unbound aggregate pavement layers. *NCHRP Synthesis 445—A Synthesis of Highway Practice*. Transportation Research Board/National Academies Press. https://doi.org/10.17226/22469

Tutumluer, E., & Seyhan, U.. (1999). Laboratory determination of anisotropic aggregate resilient moduli using an innovative test device. *Transportation Research Record*, *1687*(1), 13–21. https://doi.org/10.3141/1687-02

Tutumluer, E., & Thompson, M. R. (1997, August 17–20). Granular base moduli for mechanistic pavement design. In F. V. Hermann (Ed.), *Aircraft/Pavement Technology in the Midst of Change*, 33–47. Seattle, WA, United States. 978-0-7844-0286-3 (ISBN-13) | 0-7844-0286-8 (ISBN-10), 1997, Soft Cover, 385.